This is a preprint, the final version is subject to change, of the American Mineralogist (MSA)
Cite as Authors (Year) Title. American Mineralogist, in press.
(DOI will not work until issue is live.) DOI: http://dx.doi.org/10.2138/am-2017-5993CCBY

**January 24, 2017, REVISION 2**

# Phillipsite and Al-tobermorite mineral cements produced through low temperature water-rock reactions in Roman marine concrete

**Marie D. Jackson[1], Sean R. Mulcahy[2], Heng Chen[3], Yao Li[4], Qinfei Li[5], Piergiulio Cappelletti[6], Hans-Rudolf Wenk[7]**

[1]*Department of Geology and Geophysics, University of Utah, Salt Lake City, Utah 84112,* USA

[2]*Geology Department, Western Washington University, Bellingham, Washington 98225, USA*

[3]*School of Materials Science and Engineering, Southeast University, Nanjing 211189, People's Republic of China*

[4]*Center for Advancing Materials Performance from the Nanoscale (CAMP-Nano), Xi'an Jiaotong University, Xi'an 710049, People's Republic of China*

[5]*School of Transportation Science and Engineering, Harbin Institute of Technology, Harbin 150090, People's Republic of China*

[6]*Dipartimento di Scienze della Terra, dell'Ambiente e delle Risorse (DiSTAR), Università degli Studi di Napoli Federico II, Naples I-80134, Italy*

[7]*Department of Earth and Planetary Sciences, University of California, Berkeley, California 94720, USA*

## ABSTRACT

Pozzolanic reaction of volcanic ash with hydrated lime is thought to dominate the cementing fabric and durability of 2000-year-old Roman harbor concrete. Pliny the Elder, however, in first century CE emphasized rock-like cementitious processes involving volcanic ash (*pulvis*) "that as soon as it comes into contact with the waves of the sea and is submerged becomes a single stone mass (*fierem unum lapidem*), impregnable to the waves and every day stronger" (*Naturalis*

*Historia* 35.166). Pozzolanic crystallization of Al-tobermorite, a rare, hydrothermal, calcium-silicate-hydrate mineral with cation exchange capabilities, has been previously recognized in relict lime clasts of the concrete. Synchrotron-based X-ray microdiffraction maps of cementitious microstructures in *Baianus Sinus* and *Portus Neronis* submarine breakwaters and a *Portus Cosanus* subaerial pier now reveal that Al-tobermorite also occurs in the leached perimeters of feldspar fragments, zeolitized pumice vesicles, and *in situ* phillipsite fabrics in relict pores. Production of alkaline pore fluids through dissolution-precipitation, cation-exchange and/or carbonation reactions with Campi Flegrei ash components, similar to processes in altered trachytic and basaltic tuffs, created multiple pathways to post-pozzolanic phillipsite and Al-tobermorite crystallization at ambient seawater and surface temperatures. Long term chemical resilience of the concrete evidently relied on water-rock interactions, as Pliny the Elder inferred. Raman spectroscopic analyses of *Baianus Sinus* Al-tobermorite in diverse microstructural environments indicate a cross-linked structure with $Al^{3+}$ substitution for $Si^{4+}$ in $Q^3$ tetrahedral sites, and suggest coupled [$Al^{3+}$+$Na^{+}$] substitution and potential for cation exchange. The mineral fabrics provide a geoarchaeological prototype for developing cementitious processes through low temperature rock-fluid interactions, subsequent to an initial phase of reaction with lime that defines the activity of natural pozzolans. These processes have relevance to carbonation reactions in storage reservoirs for $CO_2$ in pyroclastic rocks, production of alkali-activated mineral cements in maritime concretes, and regenerative cementitious resilience in waste encapsulations using natural volcanic pozzolans.

Keywords: phillipsite, Al-tobermorite, Roman concrete, natural pozzolan, water-rock reaction

## INTRODUCTION

Roman marine concrete structures, composed of a volcanic ash-hydrated lime mortar that binds conglomeratic tuff or carbonate rock aggregate (*caementa*), have remained intact and coherent for 2000 years, either fully immersed in seawater or partially immersed in shoreline environments (Brandon et al. 2014). The extraordinary longevity of the concrete seems to result from the long-term durability of poorly-crystalline, calcium-aluminum-silicate-hydrate (C-A-S-H binder) in the cementing matrix of the mortar (Jackson et al. 2013a), the sequestration of chloride and sulfate ions in discrete crystalline microstructures (Jackson et al. 2012) and, as reported here, pervasive crystallization of zeolite and Al-tobermorite mineral cements in pumice clasts, dissolved feldspar crystal fragments and relict voids of the cementing matrix (Fig. 1f, g, h, j)..

The mortar of Roman marine concrete is considered the prototype of modern concretes that partially replace Portland cement with natural pozzolan to reduce $CO_2$ emissions and produce resilient C-A-S-H binder (Snellings et al. 2012). Ancient Roman concretes also have C-A-S-H binder, but it was produced through reaction of seawater, lime (CaO) calcined from limestone, and zeolitized volcanic ash, mainly from Campi Flegrei volcano (Fig. 2) (Stanislao et al. 2013; Jackson et al. 2013a; 2014). C-A-S-H is the poorly crystalline analog of Al-tobermorite, a rare, layered, calcium-silicate hydrate mineral composed of aluminosilicate chains bounded by an interlayer region and a calcium oxide sheet (e.g. Komarneni and Roy 1983; Taylor 1992; Richardson 2014; Myers et al. 2015a). Al-tobermorite does not occur in conventional concretes but occurs routinely in the relict lime clasts of Roman marine concrete (Jackson 2014) and, occasionally, in hydrothermally altered volcanic rocks (Figs. 3, 4). Al-tobermorite also occurs as an alteration product at the cement–rock interface of toxic and nuclear waste repositories (e.g. Gaucher and Blanc 2006; Lalan et al. 2016). Tobermorite group minerals have a basal interlayer

spacing of ~11 Å and an orthorhombic sub-cell symmetry with the general formula, $Ca_{4+x}(Al_ySi_{6-y})\ O_{15+2x-y}\cdot 5H_2O$, where x=1 and y=2 (Biagioni et al. 2015). Most geological occurrences have $Al^{3+}$substitution for $Si^{4+}$ in tetrahedral sites, and the generalized mineral formula, $\{[Ca_4(Si_{5.5}Al_{0.5}\ O_{17}H_2)]\ Ca_{0.2}\cdot Na_{0.1}\cdot 4H_2O$ (Taylor 1992)}, contains sodium and potassium as interlayer cations (Figs. 3b, 4b). Substitution of $Al^{3+}$ for $Si^{4+}$ in Al-tobermorite synthesized at 80–240 °C also produces ion-exchange behavior for certain radionuclides and heavy metals as interlayer cations (Komarneni and Roy 1983; Komarneni et al. 1987; Trotignon et al. 2007; Coleman et al. 2014). The crystals could prove useful in cementitious barriers and for nuclear and hazardous waste treatment and disposal if they could be produced in sufficient quantities at low temperature and, potentially, through regenerative, *in situ* cementitious processes over long periods of time.

Natural pozzolans are siliceous and aluminous earth materials, such as volcanic rock, zeolite minerals, opaline chert and shale, and diatomaceous earths. They form part of a broader class of supplemental cementitious materials (SCMs), such as fly ash, a waste product from coal-fired power plants, now incorporated in environmentally-friendly cement and concrete technologies (Lothenbach et al. 2011). Pozzolans are defined as materials "which, in themselves, possess little or no cementitious value but which will, in finely divided form and in the presence of water, react chemically with calcium hydroxide (portlandite, $Ca(OH)_2$) to form compounds possessing cementitious properties" (Mehta 1987). Pozzolanic activity is measured through various chemical tests, which determine a material's reactivity with portlandite and the rate at which it binds $Ca(OH)_2$ in the presence of water (Massazza 2004), as well as mechanical tests, which measure compressive strength over 28 days, for example, as a means to predict long term performance (ASTM-C618 2012). When finely ground these natural or artificial pozzolanic

93 materials are mixed with Portland cement to produce a blended cement paste that binds largely
94 inert sand- and gravel-sized aggregates. Blended cement pastes generally have a more refined
95 pore structure, increased chemical resistance to the ingress and deleterious action of aggressive
96 solutions, such as seawater, and to expansive alkali-silica reactions associated with reactive
97 aggregates that degrade concretes worldwide (e.g. Massazza 2004; Mehta and Monteiro 2015, p.
98 169–172), as compared with ordinary Portland cement paste. Although reliable large-scale
99 production of concretes with natural pozzolans has not been fully mastered relative to those with
100 SCMs such as fly ash, recent reductions in fly ash production and availability are now driving
101 new interest in volcanic rock pozzolans (e.g. Celik et al. 2014; Cai et al. 2016).
102 The life cycle of Roman harbor concretes structures is about two orders of magnitude
103 greater than Portland-type cement seawater concretes. Cement-based concretes are designed to
104 hydrate quickly and maintain durability through a general absence of long term cementitious
105 evolution or solubility. In maritime environments, however, the concrete commonly begins to
106 decay after a few decades due, in part, to corrosion of steel reinforcement (Mehta 1990). The
107 steel reinforcement counterattacks the relative low tensile strength and ductility of the concrete
108 and, therefore, is a structural requirement. Although concretes with pozzolanic blended cements
109 generally have reduced calcium hydroxide content relative to conventional concretes with
110 Portland cement alone, the presence of calcium hydroxide as free portlandite may persist for long
111 periods of time depending on the wt % addition of SCM (Goñl et al. 2005). Highly alkaline pore
112 solutions may thus persist indefinitely and, in the absence of chloride ions in solution, the
113 protective film on steel remains stable as long as solution pH ≥ 11.5 (Mehta and Monteiro 2014,
114 p. 179). Interaction of seawater with marine concrete corrodes steel, however, and also may
115 produce expansive reactions with calcium hydroxide (Massazza 1985). By contrast, portlandite is

116 rapidly consumed in Roman pyroclastic rock concrete reproductions, and there is no steel
117 reinforcement in the ancient structures; the volcanic ash mortars show greater ductility and bind
118 a conglomeratic rock framework that reinforces the concrete at the structural scale (Brune et al.
119 2013; Jackson 2014; Jackson et al. 2014). Roman marine concrete structures throughout the
120 Mediterranean region contain reactive, alkaline, fine sand- to gravel-sized, pumiceous ash
121 aggregate, commonly with zeolite textures, and the massive harbor structures have been left open
122 to seawater ingress for two millennia. Although pozzolanic processes in the ancient concrete
123 have been described (Jackson et al. 2013a), little is known about post-pozzolanic cementitious
124 processes that could benefit chemical resilience long after calcium hydroxide was fully
125 consumed through pozzolanic reaction with the volcanic ash aggregate.
126 Vitruvius, a Roman architect and engineer writing about 30 BCE, described this
127 pozzolanic reaction and the "latent" heat released when tuff, pumiceous ash, and lime (CaO)
128 (*tofus*, *pulvis*, and *calyx*) from the Campi Flegrei and Vesuvius volcanic districts "come into one
129 mixture and suddenly take up water and cohere together" (*de Architectura* 2.6.1–4) (Table A1).
130 An adiabatic model of exothermic heat evolved during hydration of lime and production of
131 pozzolanic C-A-S-H binder in a 10 $m^2$ by 6 m tall *Baianus Sinus* breakwater in the Bay of
132 Pozzuoli, Italy (Fig. 2, location 4), indicates that elevated temperatures, 65–95 °C, persisted for
133 2–3 years (Jackson et al. 2013a). In partially dissolved relict lime clasts, crystallization of Al-
134 tobermorite associated with C-A-S-H likely accompanied this pozzolanic phase of reaction,
135 which apparently terminated early in the history of the maritime concrete structures. In a Roman
136 concrete breakwater reproduction, for example, portlandite was fully consumed after 5 years of
137 hydration in seawater (Oleson et al. 2006; Gotti et al. 2008; Jackson 2014), similar to other
138 experimental seawater concretes with volcanic ash aggregates (Massazza 1985).

Roman natural scientists, Seneca (4 BCE–64 CE) and Pliny the Elder (70–79 CE), used geologic analogs to explain the longer term cohesion of the maritime concretes, beyond that observed by Vitruvius (Table A1). Pliny called upon the natural capacity of alkaline volcanic ash to react with water, quickly promote lithification, and, by analogy, produce rock-like qualities of endurance in marine concrete: "as soon as [volcanic ash (*pulvis*)] comes into contact with the waves of the sea and is submerged becomes a single stone mass (*fierem unum lapidem*), impregnable to the waves and every day stronger" (*Naturalis Historia* 35.166). The volcanic rock-fluid interactions inferred by Seneca and Pliny are recorded by authigenic mineral textures in the pumiceous mortar fabric of submarine and subaerial marine concrete structures. These occur in the dissolved perimeter of feldspar crystals (Fig. 1g), pores of the cementing matrix (Fig. 1b), and pumice vesicles (Fig. 1j).

To investigate these rock-like cementitious processes we compare electron probe microanalysis compositions of phillipsite, a potassic, sodic, and/or calcic zeolite, and Al-tobermorite that formed in the volcanic deposits that Romans used as aggregates with analogous crystals that formed in the marine concrete (Figs. 3, 4). We map Roman cementitious microstructures with synchroton-based X-ray microdiffraction (Figs. 5–9) to describe *in situ* zeolite and Al-tobermorite textures in the *Portus Cosanus* subaerial pier and the *Baianus Sinus* and *Portus Neronis* submarine breakwaters (Fig. 2). We then use Raman spectroscopy to identify bonding environments in *Baianus Sinus* Al-tobermorite from a variety of crystallization environments. Comparison of these spectra with those previously determined for ideal tobermorite give a qualitative measure of the role of aluminum in a cross-linked crystal structure (Figs. 10–12). The integrated results provide new insights into the low temperature crystallization and stability of phillipsite and Al-tobermorite in alkaline aqueous environments

and illustrate the beneficial role of authigenic mineral cycling in construction materials with natural volcanic pozzolan over very long service lives.

## MATERIALS AND ANALYTICAL METHODS

Roman harbor concrete structures were constructed from about 55 BCE to 115 CE, and cored by the ROMACONS drilling program from 2002 to 2006 (Brandon et al. 2014). The conglomeratic concrete cores contain about 40–45 volume% zeolitized tuff coarse aggregate, and 55–60 volume% pumiceous volcanic ash-hydrated lime mortar. The marine concrete is exposed sub-aerially at *Portus Cosanus* (PCO.03.01), Orbetello, (42.4079˚ N, 11.2933˚ E), and submerged in seawater at *Baianus Sinus* (BAI.06.03), Bay of Pozzuoli, (40.8228˚ N, 14.0885˚ E), *Portus Neronis* (ANZ.02.01), Anzio, (41.4432˚ N, 12.6314˚ E) and *Portus Traianus* (PTR.02.02), Ostia (41.7785˚ N, 12.2520˚ E).

### Electron Probe Microanalysis (EPMA)

Samples were analyzed with a Cameca SX-51 electron microprobe equipped with five wavelength dispersive spectrometers using a 15 keV accelerating voltage, a 10 nA beam current, and a 1-2 μm beam diameter. Counting time was 10 s on peak and background for all elements. Major element compositions of phillipsite and clusters of 1–5 μm Al-tobermorite were acquired from polished thin sections of tuffs and mortars prepared according to hydrophobic specifications. New determinations of phillipsite compositions in Campi Flegrei Bacoli Tuff (BT) and Neapolitan Yellow Tuff (NYT) deposits and of phillipsite and Al-tobermorite compositions in the marine mortars are compared with previously published compositions (Figs. 3, 4; Tables 1, 2, S1). The BT sample comes from an unidentified quarry near Fondi di Baia, at about 40.80˚ N, 14.07˚ E; the NYT samples come from outcrops in Naples at 40.89˚ N, 14.18˚ E. To account for potential Na and K loss and/or Si and Al gain, a time dependent intensity

185 calibration was also applied to these elements using the software Probe for EPMA (e.g., Meier et
186 al. 2011). Oxygen and water content were calculated by stoichiometry. Uncertainties in the
187 weight percent oxides were determined by counting statistics and propagated through the
188 calculation of formula units (Giaramita and Day 1990). The fine grain size of Al-tobermorite
189 contributed to lower wt % oxide measurements. Analyses with wt% oxide totals < 80 (with $H_2O$
190 calculated by stoichiometry) and low atoms per formula unit were omitted from Table 2. Areas
191 with visible traces of calcium carbonate crystals were not analyzed. Plotting coordinates for
192 ternary diagrams were calculated from the mineral formulas of phillipsite and Al-tobermorite.
193 The Si-$D_{0.25}Al_{0.50}Si_{0.50}$ – $M_{0.50}Al_{0.50}Si_{0.50}$ molecular proportions were calculated as Si = Si – Al;
194 $D_{0.25}Al_{0.50}Si_{0.50}$ = 2(2Al(Ca + Mg + Ba + Sr)))/((Na + K) + 2(Ca + Mg + Ba + Sr)); M = 2(Al(Na
195 + K))/((Na + K)+2(Ca + Mg + Ba + Sr)), where D and M refer to divalent and monovalent
196 cations, respectively (Deer et al. 2004; Gatta et al. 2010). The plotting coordinates of other
197 ternary diagrams are based on molecular proportions as defined at the apices of a given diagram.
198 **Synchroton based X-Ray Microdiffraction**
199 Crystalline phases in *Portus Cosanus* and *Baianus Sinus* cementitious microstructures
200 were determined at Advanced Light Source beamline 12.3.2 at Lawrence Berkeley National
201 Laboratory (Tamura et al. 2009) with microdiffraction and microfluoresence analyses (Figs. 5–
202 8). Polished thin sections were prepared using superglue adhesive, studied with petrographic
203 methods, and then detached from the glass slide by soaking in nitromethane. The 0.3 mm thick
204 mortar slice was then mounted on adhesive tape and loaded in transmission mode into the beam,
205 with the detector tilted at 30° – 39° to the incident beam. A monochromatic X-ray beam of 8 or
206 10 KeV was focused to a 2 by 5 $\mu m^2$ diameter spot size. A Pilatus 1M area detector placed at 150
207 mm recorded Debye rings diffracted by crystalline phases. Debye rings at successive d-spacing

208 reflections were integrated radially for 2θ, 3° up to 54°, over an arch segment around the cone of
209 diffraction of up to 76° to create intensity versus d-spacing plots. These are shown as q, 2π/d-
210 spacing, to increase readability of low d-spacing reflections.

211 **Scanning Electron Microscopy (SEM)**

212 Compositional high resolution energy dispersive X-ray spectroscopy (EDS) elemental
213 maps of the same *Portus Cosanus* and *Baianus Sinus* microstructures were obtained with a
214 Bruker Xflash 5060F Silicon Drift Detector (SDD) on a Zeiss Merlin Compact Scanning
215 Electron Microscope (SEM) at the Bruker Laboratories in Berlin, Germany (Figs. 7, 9). Element
216 concentrations are displayed by quantitative mapping (QMap) in normalized mass% using the
217 PB-ZAF quantification method. Element distributions are shown in false color display from
218 black to blue, green, yellow to red, with the highest mass% concentration. Noise was removed by
219 adjusting the maximum intensity threshold for each element. The analyses utilized high voltage,
220 8 KeV, resolution of 379 nm per pixel, and 196 µs residence time (Fig. 7b, c), 197 nm per pixel,
221 88 µs (Fig. 7f, g), and 10 KeV, 388 nm per pixel, 312 µs (Fig. 7k–n). Backscattered (BSE)
222 images of tuffs and mortars (Figs. 1b-d, f-j, 6, 7a-c, 8a-c, 9a, b) were acquired with the Zeiss
223 EVOMA10 Scanning Electron Microscope at the UC Berkeley Department of Earth and
224 Planetary Sciences. A secondary electron image (Fig. 1e) of Surtsey tuff from a 1979 drill core
225 was acquired by J. G. Moore in 1979 using an ARL-EMX microprobe at the U. S. Geological
226 Survey, Menlo Park, California.

227 **Raman spectroscopy**

228 Raman spectra obtained through a confocal microscope is correlated with crystals in
229 cementitious microstructures previously analyzed with X-ray microdiffraction in *Baianus Sinus*
230 relict lime clasts, pumice clasts, and relict voids (Figs. 10–12, Table 3). A JYHoriba LabRAM

spectrometer at the Department of Chemical Engineering, UC Berkeley, was used in backscattering configuration, with HeNe laser (632.8 nm) excitation line, power at ~5 mW, and through an 100X confocal microscope (aperture= 0.8; laser spot size <1μm). The spectra evaluate the nearest neighbor bonding environments of the silicate tetrahedron via oxygen corresponding to $Q^n$ (*m* Si (or Al)), where $Q^n$ silicate tetrahedra are connected via *n* bridging oxygens to *m* $Si^{4+}$ (or $Al^{3+}$). Bands at 1074, 1086, etc. indicate C–O stretching in calcite and vaterite (Black et al. 2007, Wehrmeister et al. 2009). No Raman spectra exist for 11Å Al-tobermorite and C-A-S-H in published literature. We therefore compare Roman syntheses of Al-tobermorite and C-A-S-H spectra with spectra of laboratory syntheses of 11Å tobermorite without aluminum, geologic 11Å tobermorite from Crestmore, California, and laboratory C-S-H with calcium/silica=0.8 to 0.83 referenced in previous NMR studies (Kirkpatrick et al. 1997; Richardson et al. 2010; Black 2009; Jackson et al. 2013a, b).

## CEMENTING FABRICS

Lithification of volcanic ash to form tuffaceous rock is one of the principal processes through which a volcano consolidates and stabilizes its deposits. Diagenetic and hydrothermal interaction of surface, ground, or seawater with volcanic ash components – glass, crystals, and lithic fragments – produces a sequence of authigenic crystalline phases that cement loose tephra to form tuff (e.g. Hay and Iijima 1968; Jakobsson and Moore 1986). In the Neapolitan Yellow Tuff (NYT), 14.9 ± 0.4 ka (Fedele et al. 2011), phillipsite and chabazite, a zeolite with more calcic compositions (de Gennaro et al. 2000), formed from alkaline hydrothermal solutions produced through interactions with volcanic glass. The crystals bind a vitric matrix, consolidate interfacial zones of pumiceous clasts, and fill relict pores and pumice vesicles; alkali feldspar crystal fragments partially dissolved and also produced zeolite textures (Fig. 1b–d). The

authigenic minerals in alkali-rich trachytic to phonolitic Campi Flegrei deposits selected by Roman engineers for marine concrete are mainly zeolites (de Gennaro et al. 2000; Jackson 2014). Indeed, phillipsite in the vesicles of pumice clasts in the mortars mainly has intermediate silica compositions that are similar to phillipsite from NYT and Bacoli Tuff (BT), 8.6 ± 0.6 ka (Fedele et al. 2011); these are shown, for example, by most *Portus Neronis* phillipsite compositions (Figs. 3a, 4a; Tables 1, S1).

Although Roman marine mortar has a mesoscale pumiceous structure that is analogous to the clastic fabric of Campi Flegrei tuff (Fig. 1f–h), the cementing matrix contains predominantly C-A-S-H binder. *In situ* dissolution of trachytic glass (Fig. 1f) and alkali feldspar crystal fragments occurred (Fig. 1g), as in the Campi Flegrei tuffs, but the reaction products are not zeolites. Dissolution of an alkali feldspar crystal fragment in the hardened cementing matrix of the *Portus Neronis* mortar, for example, produced a 100 $\mu m^2$ mold (Fig. 5). Al-tobermorite and strätlingite, a hydrated calcium-aluminum phyllosilicate ($Ca_2Al_2(SiO_2)$ $(OH)10•2.5(H_2O)$, with 12.5 Å (0001) basal spacing, crystallized along the perimeter of the remnant feldspar crystal. Dissolution evidently raised solution ionic concentrations in the mold, and hydrate precipitation occurred in a leached layer behind the dissolution front (Snellings 2015). Feldspar compositions in the mortars range from potassic (9–12 wt % $K_2O$, 1–2 wt % $Na_2O$ and CaO) to more sodic (5–7 wt % $K_2O$, 3–5 wt % $Na_2O$ and 1–2 wt % CaO).

Vesicles in the perimeter of a pumice clast in the subaerial *Portus Cosanus* mortar contain deeply etched, 15–20 μm Campi Flegrei phillipsite crystals surrounded by C-A-S-H and sub-spherical accumulations of ~5 μm Al-tobermorite (Fig. 1i, locations [1], [2], [3])). These microstructures record deep dissolution of Campi Flegrei phillipsite [1], production of pozzolanic C-A-S-H and Al-tobermorite [2, 3], and abrupt termination of pozzolanic reaction

before the phillipsite was fully consumed. Experimental mixing of portlandite with phillipsite in Neapolitan Yellow Tuff by Mertens et al. (2009) provides insight into these microstructures. Rapid pozzolanic reaction occurred for a few days until thickening of a reaction rim of hydrates covered the external surfaces of the crystals; the reaction then slowed considerably at 10 day's hydration and proceeded through a diffusion controlled process. The *Portus Cosanus* pumice vesicles evidently record rapid pozzolanic reaction through pH 12–14 pore solutions derived from seawater, calcium hydroxide, and trachytic ash, as Vitruvius described (Table A1), but sealing of the surfaces of the phillipsite crystals by C-A-S-H and Al-tobermorite hydration products prevented further pozzolanic reaction. Remarkably, the center of this vesicle and adjacent vesicles (Fig. 6a, location [4]) contain masses of <1–2 μm Al-tobermorite crystals, identified through X-ray microdiffraction. These very fine-grained, irregularly shaped agglomerations of Al-tobermorite, which occur as moderate brown, opaque zones in plane polarized light and cloudy light gray areas in SEM-BSE (Fig. 6b, c), seem to have formed subsequently to the sub-spherical accumulations of coarse-grained, pozzolanic Al-tobermorite.

The fine-grained agglomerations of Al-tobermorite in pumice vesicles of the *Portus Cosanus*, *Portus Neronis* (Fig. 6b, c) and *Baianus Sinus* mortars are commonly associated with sub-rounded phillipsite aggregations and etched or frayed alkali feldspar crystal fragments. In *Portus Neronis* and *Baianus Sinus* pumice vesicles, Al-tobermorite contains 43.2–47.6 wt% $SiO_2$. These compositions are more siliceous than those of crystals that formed in relict lime clasts in the same mortar specimens, and they show a greater range of $Al_2O_3$ and CaO contents (Figs. 3b, 4b, Table 2). Some compositions are nearly identical to Al-tobermorite that crystallized in 15-year-old basaltic tuff of Surtsey volcano, Iceland (Jakobsson and Moore 1986). $Na_2O$ and $K_2O$ at 1.2–3.0 wt% throughout partially balance $Al^{3+}$ substitution for $Si^{4+}$ relative to

ideal tobermorite (Mitsuda and Taylor 1978; Taylor 1992; Barnes and Scheetz 1991; Komarneni and Roy 1983). These compositions and the fine-grained habit of the crystals suggest a possible post-pozzolanic origin. They may have precipitated from alkaline fluids in more or less closed chemical systems in vesicles, produced through reaction of feldspar crystals, potassic phillipsite, and trachytic glass, which contains up to 12 wt% $Na_2O + K_2O$ and 2–3 wt% CaO (de Gennaro et al. 2000; Fedele et al. 2011).

Although one might suppose that all zeolite in the mortars has a geological origin, phillipsite textures in relict voids of the cementing matrix indicate *in situ* crystallization (Fig. 1h). X-ray microdiffraction analyses of *Baianus Sinus* mortar show, for example, phillipsite clusters that crystallized on Al-tobermorite plates in the cementing matrix (Jackson et al. 2013b). Compared with most Campi Flegrei phillipsite, the phillipsite that formed in relict pores of the marine mortar has lower silica ($SiO_2$, 38–45 wt%), higher alumina ($Al_2O_3$, 28–31 wt%), lower Si/Al (1.3–1.6), and greater calcium (CaO, 7–11 wt%) (Figs. 3a, 4a, Tables 1, S1). In volcanic deposits and saline lakes, phillipsite crystallizes from pH 8–10 pore fluids (Hay and Iijima 1968; Taylor and Surdam 1981; de Gennaro et al. 2000, Sheppard and Hay 2001); crystal compositions vary with silica activity, salinity, and alkalinity in the fluid phase. Alumina content in phillipsite increases with higher pH pore fluids, but this pH is substantially lower than that of pozzolanic fluids with pH > 12, which are buffered by calcium hydroxide (Lothenbach et al. 2011).

**Maps of post-pozzolanic cementitious microstructures**

Synchrotron-based X-ray microdiffraction maps and high resolution SEM-EDS compositional maps of *Portus Cosanus* and *Baianus Sinus* microstructures provide further insights into diverse pathways for Al-tobermorite crystallization in the Roman mortar fabrics (Fig. 7). In the subaerial *Portus Cosanus* pier intermittently exposed to ingress of seawater and

meteoric water, Campi Flegrei phillipsite aggregations that line the vesicle surfaces of a pumice clast have a sub-rounded form with 2–3 μm alteration rims, and/or they are altered to vaterite or calcite; the adjacent chabazite is mainly intact (Figs. 7a–d). Fine-grained agglomerations of 1–2 μm Al-tobermorite occupy the calcium-enriched internal space of the pumice vesicle, along with vaterite, a metastable calcium carbonate (Fig. 8a, b). The Al-tobermorite has large (002) interlayer spacing, 11.41–11.47 Å, indicating substantial $Al^{3+}$ for $Si^{4+}$ (Barnes and Scheetz 1991) (Fig. 7i (analysis *C*)). A nearby vesicle, however, has Campi Flegrei chabazite and phillipsite that are more strongly altered to vaterite and calcite (Fig. 7e–h). There, calcium-enriched areas on the SEM-EDS maps correlate with zeolite alteration to vaterite and calcite; no Al-tobermorite is present. Instead, there are occasional strätlingite crystals (Figs. 7i (analysis *D*); 8c, d). The rounded forms of the phillipsite aggregations (Figs. 7a, 8a), where individual crystal laths have disappeared compared with intact aggregations (Figs. 1h, 9b), suggest possible cation exchange processes. The porous, open, silicate framework of the crystals has a large internal space available for reaction, and repeated cation exchanges occurring along the external surfaces of the laths can decrease the silicate framework, causing the protruding crystals to decompose (Hay 1966). The exchangeable cation reactions would have had a strong influence on alkali concentrations and compositions of solutions within the vesicles, and their crystalline precipitates (Mertens et al. 2009). Overall, the microstructures indicate low-temperature, post-pozzolanic reactions involving zeolite in Campi Flegrei pumice within relatively closed chemical systems at the vesicle scale.

In *Baianus Sinus* breakwater continually submerged in seawater for 2000 years, the cementing matrix of the mortar contains relict, submillimeter-sized pores filled with 100–200 μm phillipsite fabrics (Fig. 7j–o). The coarse-grained fabrics formed *in situ*, perhaps associated with

346 alkaline fluids produced by dissolution within a nearby Campi Flegrei vitric tuff clast. SEM-EDS
347 analyses indicate aluminous compositions with 11 wt% potassium and 6 wt% sodium.
348 Hydrocalumite, a platey calcium chloroaluminate ($Ca_2Al(OH)_{6.5}Cl_{0.5}•3(H_2O)$), filled the center
349 of the relict voids (Fig. 9a, b). Although much of the phillipsite remains intact, areas of higher
350 sodium and sulfur concentrations coincide with X-ray microdiffraction analyses indicating
351 newly-formed cementitious hydrates, mainly ettringite and Al-tobermorite (Fig. 9d, e). Ettringite,
352 a hydrous calcium-aluminum-sulfate ($Ca_6Al_2(SO_4)_3(OH)_{12}•26(H_2O)$), crystallized in zones with
353 higher sulfur concentrations. Al-tobermorite crystallized in narrow zones with higher calcium
354 and lower silica contents. The acicular crystals protrude from the etched surfaces of the
355 phillipsite fabrics into relict pore space (Fig. 1j). This interfacial relationship is illustrated by X-
356 ray microdiffraction patterns showing both phillipsite and Al-tobermorite at the submicron scale
357 (Fig. 9c, d, locations #54, #57). Similar phillipsite and Al-tobermorite mineral assemblages have
358 been described in basaltic tuff at Surtsey volcano, Iceland, at 100 °C fifteen years after eruption
359 (Jakobsson and Moore 1986) (Fig. 1e). The *Baianus Sinus* microstructures demonstrate that Al-
360 tobermorite crystallization can occur at ambient seawater temperatures, 14–26 °C (Damiani et al.
361 1987), in a highly potassic and sodic system produced through alteration of phillipsite, which
362 itself precipitated in the mortar fabric. The complex mineral textures indicate cycling of low-
363 temperature, post-pozzolanic reactions in pores of the cementing matrix as a response to
364 evolving fluid interactions over time.

365 **RAMAN SPECTROSCOPY**

366 Raman spectroscopic analyses referenced to previous $^{29}Si$ and $^{27}Al$ Nuclear Magnetic
367 Resonance (NMR) studies provide insights into the roles of $Al^{3+}$, $Na^+$, and $K^+$ in *Baianus Sinus*
368 Al-tobermorite from diverse microstructural environments, as compared with ideal tobermorite

369 {$Ca_5Si_6O_{17}\cdot 5H_2O$ (Biagioni et al. 2015)}, *Baianus Sinus* C-A-S-H, and calcium-silicate-hydrate
370 C-S-H binder (Figs. 10–12). X-ray microdiffraction analyses of Al-tobermorite in relict lime
371 clasts, pumice clasts, and relict voids show rather uniform patterns, with 11.20–11.24 Å
372 interlayer spacing, modified mainly by the relative intensity of vaterite and calcite reflections
373 (Fig. 10a). Raman spectra of the same or adjacent crystals mainly show a 670–671 $cm^{-1}$ band
374 corresponding to symmetrical bending (SB) of $Q^2$(0Al) linkages of middle chain silicon
375 tetrahedra (Kirkpatrick et al. 1997; Richardson et al. 2010) (Fig. 10b). A sharp 1111–1112 band
376 indicates symmetrical stretching (SS) of bridging $Q^3$(1Al) linkages (Richardson et al. 2010).
377 These linkages are shown in NMR study of *Baianus Sinus* Al-tobermorite in relict lime clasts
378 (Jackson et al. 2013a, b) (Fig. 12); the ~1040–1080 band associated with SS $Q^3$(0Al) is,
379 however, obscured by carbonate bands. A 638–642 band corresponds to SB of $Q^3$(0Al)
380 (Kirkpatrick et al. 1997) and $Q^3$(1Al). The SB and SS $Q^3$ bands indicate linkages across the (002)
381 interlayer, which contains channels for water molecules and exchangeable alkali cations (Tsuji
382 and Komarneni 1989; Yamazaki and Toraya 2001). A ~840–900 shoulder indicates SS of
383 $Q^1$(0Al) sites (McMillan and Piriou 1982). A prominent 800–840 maximum not detected in ideal
384 tobermorite (Fig. 11) may indicate both Al–O stretching and $Q^1$ motions of silica and aluminum
385 against tetrahedral oxygen (McMillan and Piriou 1982).

386 Roman Al-tobermorite spectra shows substantial variation from the spectra of ideal
387 tobermorite (Fig. 11, Tobermorite [1],[2]). In ideal tobermorite, SS $Q^2$ linkages assigned to 950–
388 1010 (Richardson et al. 2010) occur as a broad band centered at 998. There is little band
389 definition, however, in Roman Al-tobermorite in this region, with the exception of analysis 7
390 (Fig. 10b), which corresponds to an X-ray microdiffraction site where Al-tobermorite
391 crystallized in the interfacial zone of *in situ* phillipsite aggregations (Fig. 9d, location #15). In

crystals and glasses of silica-alumina systems, highly condensed aluminate tetrahedra may lead to geometric distortion, loss of vibrational coherence and observed band structure (McMillan and Piriou 1982; McMillan et al. 1982). Substantial $Q^2$(1Al) relative to $Q^2$(0Al) occurs in $^{29}$Si and $^{27}$Al NMR study of Roman Al-tobermorite in relict lime clasts (Fig. 12), as well as in cross-linked Al-tobermorite synthesized pozzolanically through pozzolanic interaction of NaOH-activated trachytic volcanic rock with calcium hydroxide (Youssef et al. 2010). This suggests that abundant $Al^{3+}$ substitution for $Si^{4+}$ may dampen the expression of the SS $Q^2$(0Al) linkages, causing loss of the SS $Q^2$ band, but quantification of these relationships is beyond the scope of this article. SS $Q^1$ in ideal tobermorite appears as a broad, low intensity band centered at 850. Roman Al-tobermorite, instead, has an asymmetric maximum at 807–840 that leads to a weak shoulder at ~840–900. The shoulder may indicate SS $Q^1$(0Al), but the maxima composed of 806–809, 821–826, and 837–842 bands may indicate a component of Al–O stretching (McMillan and Piriou 1982; McMillan et al. 1982), which occurs at 796–804 and 841 in certain calcium-alumina-silicate crystals (Sharma et al. 1982). NMR studies of sodic and potassic C-A-S-H (C-(N, K-)A-S-H) show increased $Q^1$ intensity with Na and K content; binding of silica to $Na^+$ and $K^+$ rather than $Ca^{2+}$ in the interlayer and the CaO surface leads to more silica dimers, shorter silicate chain lengths, and increased $Q^1$ (Myers et al. 2015b; L'Hôpital et al. 2016). A +3 ppm shift of $Q^3$(1Al) in $^{29}$NMR study of Roman Al-tobermorite (Fig. 11) also suggests a greater proportion of monovalent cations relative to $Ca^{2+}$ (Myers et al. 2015b). The Al-tobermorite 800–840 maxima may thus correspond to complex $Q^1$(0Al) and $Q^1$(1Al) sites and, perhaps, coupled $[Al^{3+}+Na^+]$ substitution, similar to laboratory syntheses in which tetrahedrally-coordinated $Al^{3+}$ substitutes for $Si^{4+}$ and $Cs^+$ selectively exchanges for $Na^+$ in the cross-linked (002) interlayer (e.g. Tsuji and Komarneni 1989; Coleman et al. 2014).

415 SB $Q^2$ in ideal tobermorite and C-S-H is assigned to 650–680 (Kirkpatrick et al. 1997,
416 Richardson et al. 2010; Black 2009). The absence of the 670–671 band in Al-tobermorite
417 associated with phillipsite alteration in relict voids where qualitative EDS analyses indicate high
418 alumina (Figs. 7j–n, 9e), suggests that condensed aluminate tetrahedra could contribute to loss of
419 the silicate band structure (McMillan and Piriou 1982; McMillan et al. 1982), as for SS $Q^2$. SB of
420 $Q^3$ linkages in ideal tobermorite is assigned to 620 (Kirkpatrick et al. 1997), apparently based on
421 a metasilicate band group at 1050, 980, and 650 and vibrational similarities with a $SiO_2$–$CaAl_2O_4$
422 glass series (McMillan et al. 1982). The 638–642 band in Roman Al-tobermorite could therefore
423 correspond to SB $Q^3$(0Al) and $Q^3$(1Al), associated with SS Q3 vibrations at 1111 and obscured
424 at 1080. $^{27}$Al NMR of crystals from relict lime clasts records these tetrahedral $Q^3$(1Al) linkages
425 through a peak at 57.70 ppm (Jackson et al. 2013a, b). Distortions of $AlO_4$ tetrahedral bond
426 lengths and complexities in Al–O coordination in Roman Al-tobermorite in relict lime clasts are
427 indicated by NEXAFS spectra, where a tetrahedral 1566.7 absorption edge broadens to an
428 octahedral 1571.0 eV absorption edge. These complexities may also be recorded by $^{27}$Al NMR,
429 which has a weak octahedrally-coordinated $Al_2O_6$ component at 10.88 ppm (Jackson et al.
430 2013a, b). Components of both Al–O stretching and complex motions of silica and aluminum
431 against tetrahedral oxygen may therefore occur at the Raman 443 and the 800–840 maxima
432 (McMillan and Piriou 1982; McMillan et al. 1982). It is not clear how these spectra might record
433 possible octahedrally-coordinated $Al^{3+}$ substitution for $Ca^{2+}$ within the interlayer of the crystals
434 (Abdolhosseini Qomi et al. 2012).

435 *Baianus Sinus* C-A-S-H shows rather uniform Raman spectra over a diverse range of
436 cementitious microstructures (Fig. 11). A broad band centered at 668 corresponds to
437 symmetrical bending (SB) of $Q^2$(0Al), and could also include SB of $Q^2$(1Al), given the

tetrahedral aluminum 1566.7 absorption edge recorded by NEXAFS spectra of C-A-S-H in relict lime clasts (Jackson et al. 2013a). SS $Q^2$ linkages occur as a broad band centered at 994. Spectra indicating SS $Q^3$(0Al) and a cross-linked structure at ~1040–1080 band are, however, obscured by carbonate bands.

## AUTHIGENIC MINERAL CYCLING

Alteration of tephra deposits occurs when interstitial water becomes modified through hydrolysis or dissolution of volcanic ash components. These reactions release hydroxyl ions, and the solution becomes more alkaline and enriched in Na, K, Ca and Si along its flow path. Zeolites crystallize when the cation to hydrogen ion ratio and other ionic activities are relatively high (Sheppard and Hay 2001). Early formed zeolites commonly alter to other zeolites; phillipsite, for example, commonly alters to analcime, and analcime can be replaced by laumontite, K-feldspar, or albite (Hay and Sheppard 2001). Authigenic textures thus record dynamic physico-chemical environments and phase stability relationships over time in open-to-closed hydrologic systems.

In Campi Flegrei deposits, post-eruptive hydrolysis and dissolution of trachytic glass in the presence of condensed water vapor generated alkaline fluids from which zeolites originated (Fig. 1b–d) (de Gennaro et al. 1999). Airfall deposits from highly expanded ash clouds with limited water-magma interaction are less zeolitized than hydromagmatic deposits that retain pore water and water vapor, grow zeolite mineral cements, and lithify to form tuff. By first century BCE, Roman engineers had identified the unconsolidated pumiceous ash deposits, or *pozzolana*, as the optimum aggregate (*pulvis*) for maritime concrete harbor mortars; they used lithified zeolitized tuff deposits as coarse aggregate (*caementa*) in the concrete (Stanislao et al. 2014; Jackson 2014). When they installed the pumiceous ash and lime mortar mixture hydrated with

461 seawater in subaerial and submarine structures, they created a highly alkaline but relatively
462 short-lived pozzolanic system buffered by calcium hydroxide, which produced C-A-S-H and Al-
463 tobermorite at ≤ 95 °C in lime clasts (Jackson et al. 2013a). Pozzolanic reaction of Campi
464 Flegrei phillipsite in the perimetral vesicles of pumice clasts in response to infiltration of the
465 high pH fluids also produced C-A-S-H and Al-tobermorite (Fig. 1i, 6a). Rates of reaction may
466 have been on the order of days or weeks, based on experimental mixing of portlandite and
467 distilled water with phillipsite at 40 °C with phillipsite from Neapolitan Yellow Tuff (Mertens et
468 al. 2009). The mortar reaction became diffusion controlled and eventually terminated when C-A-
469 S-H and Al-tobermorite accumulations enveloped the phillipsite aggregations. Consumption of
470 portlandite in the large Roman harbor structures was likely complete within 5–10 years, based on
471 an experimental concrete reproduction (Oleson et al. 2006, Jackson 2014), an adiabatic model of
472 heat evolved in the *Baianus Sinus* breakwater (Jackson et al. 2013a), and observations of
473 pozzolanic systems with pyroclastic rock pozzolans (Massazza 1985; 2004). This is in contrast to
474 Portland cement concretes which maintain very high pH and alkalinity over the long term, since
475 portlandite saturation and free portlandite in pore fluids persist for extended periods of time.

476 In the post-pozzolanic hydrologic system of the massive Roman concrete structures open
477 to seawater and/or meteoric water ingress, residual components of the pumiceous ash – feldspar
478 crystal fragments, authigenic phillipsite, and trachytic glass – reacted with interstitial fluids at
479 low temperature to produced alkaline pore solutions in diverse components of the mortar fabric.
480 Al-tobermorite (and strätlingite) crystallized in the leached perimeters of Campi Flegrei feldspar
481 fragments (Figs. 1g, 5) and in pumice vesicles in response to dissolution or decomposition of
482 Campi Flegrei phillipsite (and chabazite) (Figs. 6, 7a–i, 8). *In situ* crystallization of phillipsite
483 occurred in relict pores throughout the cementing matrix (Figs. 1h, 7j–o, 9), apparently at

ambient seawater temperatures, 14–28 °C, after exothermic heat evolution through pozzolanic reaction was complete. Al-tobermorite then crystallized in the interfacial zones of these phillipsite fabrics. These crystals resemble those that crystallized from dissolving phillipsite in 15-year-old palagonitized basaltic tuff of Surtsey volcano, Iceland, but at 100 °C (Fig. 1e, i).

Al-tobermorite is considered to have a hydrothermal origin in geologic occurrences (Claringbull and Hey 1952; Mitsuda and Taylor 1978; Livingstone 1988; Henmi and Kusachi 1992; Hoffman and Armbuster 1997; Aguirre et al. 1998) and has been previously produced in laboratory syntheses always at ≥ 80 °C (e.g. Komarneni and Roy 1983). Alkali-activated pozzolanic production of zeolite and Al-tobermorite has been produced in autoclaved aerated concrete, heated at 110–200 °C in 12 hours to 7 days (Grutzeck et al. 2004), and through NaOH-activation of trachytic rock aggregate mixed with calcium hydroxide and heated at 150–175 °C for 24 hours (Youssef et al. 2010). Relatively low temperature crystallization of phillipsite and Al-tobermorite has occurred, however, in the pores of Portland cement paste in contact with a claystone interface at 70 °C one year after installation (Lalan et al. 2016). Furthermore, Al-tobermorite has been identified throughout a 181 m core drilled through Surtsey in 1979, at temperatures from 25 °C in surficial deposits to 140 °C in hydrothermally-altered tuff (Jakobsson and Moore 1986) (see Fig. 1e). The distinguishing feature of the Roman marine mortar system is to record low temperature processes of authigenic mineral cycling, which involve reaction of volcanic ash components; production of alkaline fluids in microenvironments; precipitation of new minerals, principally phillipsite in these microstructures; and evolving pore solution chemistries that produce Al-tobermorite crystallization in subaerial and submarine structures.

Systems that begin as relatively simple states and evolve to states of increasing complexity are a recurrent characteristic of mineral evolution and Earth processes, as well as

emerging technologies (Hazen et al. 2008). Vitruvius described the relatively simple mixture of volcanic ash (*pulvis*), lime (*calx*) and tuff aggregate (*tofus*) that cohered pozzolanically in seawater. Pliny the Elder and Seneca called upon geologic analogs to explain concrete resilience after 100–150 years of service life. Advanced analytical techniques now show the complexity of Roman marine concrete technologies, whose initial protocols for developing an effective pozzolanic cementitious system evolved through authigenic mineral cycling to produce cementitious systems with the range of water-rock interactions and longevity of pyroclastic deposits in Earth's upper crust. Roman builders evidently had these objectives in mind when designing the maritime concrete structures (Brandon et al. 2014).

The cementing fabrics of Roman concrete breakwaters and piers constructed with volcanic ash mortars provide a well-constrained template for developing cementitious technologies through low temperature rock-fluid interactions, cation-exchange, and carbonation reactions that occur long after an initial phase of reaction with lime that defines the activity of natural pozzolans (Massazza 2004). Some aspects of the Roman post-pozzolanic system have been reproduced by geopolymer-type cementitious systems, where alkali mediated dissolution and precipitation reactions involving little or no calcium occur in aqueous reaction substrates (Provis and Bernal 2014). These systems do not, however, produce on-going beneficial precipitation of cementitious hydrates through evolving alteration of reactive aggregate(s). Coupled dissolution and precipitation processes produced through the reactivity of synthetic calcium (alumino)silicate glasses, basaltic glasses, and borosilicate glasses with aqueous solutions at varying pH (Snellings 2015; Jantzen et al. in press) have a great deal of relevance for gaining further understanding of multiple pathways to low-temperature Al-tobermorite crystallization. This especially concerns variable solution chemistries produced in

microenvironments associated with authigenic dissolution of the alkaline components of pozzolanic volcanic ash — alkali feldspar, trachytic glass, and relict zeolite textures. Carbonation of zeolite in the pumice clasts of the subaerial mortar also apparently released alkaline earth elements associated with low-temperature crystallization of Al-tobermorite. The platy and acicular Al-tobermorite crystals, may increase ductility and resistance to fracture (Jackson et al. 2104), possibly leading to the increasing mechanical resilience of these concrete that Pliny observed (…and stronger every day (*fortiorem cotidie*) (Table A1)).

## IMPLICATIONS

That *in situ* production of alkaline pore fluids derived from low-temperature interactions of seawater-derived fluids with components of trachytic Campi Flegrei pumiceous ash drives zeolite and Al-tobermorite crystallization in Roman marine concrete is a surprising discovery, since 1) laboratory Al-tobermorite syntheses have not been produced at ambient temperatures, and 2) release of alkali cations from rock aggregate in Portland cement concrete generally produces expansive alkali-silica gels that degrade structural concretes worldwide. By contrast, the alkaline fluids in Roman subaerial and submarine concrete piers and breakwaters produce precipitation of phillipsite and Al-tobermorite mineral cements that refine pore space, enhance bonding in pumice clasts and sequester alkali cations, principally sodium and potassium.

Roman marine concretes can provide guidelines for the optimal selection of natural volcanic pozzolans that have the potential to produce of regenerative cementitious resilience through long term crystallization of zeolite, Al-tobermorite, and strätlingite mineral cements. The cross-linked structure and $Al^{3+}$ bonding environments of the Roman Al-tobermorite crystals, recorded by Raman spectra through a range of cementitious microstructures and crystallization pathways, provide clues to creating new pathways for cation-change in high performance

concretes. Furthermore, the chemical and mechanical resilience of the marine concrete provides keys to understanding dynamic mineral cements in young, oceanic pyroclastic deposits, as at Surtsey (Jakobsson and Moore 1986), the seismic response of a volcanic edifice, as in deep Campi Flegrei deposits (Vanorio and Kanitpanyacharoen 2015), and carbon mineralization reactions, as occur in porous basaltic storage reservoirs for anthropogenic $CO_2$ (Matter et al. 2016). Roman prototypes for brine-based concretes could conserve freshwater resources, generate multiple low temperature pathways to pozzolanic and post-pozzolanic Al-tobermorite sorbents with coupled $Al^{3+}$ and exchangeable alkali cation sites, and extend applications of natural volcanic pozzolans to environmentally-friendly, alkali-activated structural concretes and cementitious barriers for waste encapsulations.

## ACKNOWLEDGMENTS

We extend special thanks to M. Patzschke, Bruker Laboratories, Berlin, and to N. Tamura and M. Kunz, Advanced Light Source (ALS) beamline 12.3.2, for assistance with the coupled compositional and X-ray microdiffraction maps of *Portus Cosanus* and *Baianus Sinus* microstructures. T. Teague and C. Carraro, U. C. Berkeley, provided analytical support. J. G. Moore, U. S. Geological Survey, shared valuable perspectives on Surtsey deposits. J. P. Oleson, C. Brandon, and R. L. Holhfelder of the ROMACONS program drilled the cores of the harbor concrete structures with support from CTG Italcementi, Bergamo, Italy. Data acquired at ALS beamlime 12.3.2. at Lawrence Berkeley Laboratories were supported by the Director of the Office of Science, Department of Energy, under Contract No. DE-AC02-05CH11231. Acquisition of Raman spectra in the UC Berkeley Department of Chemical Engineering was funded by National Science Foundation SUSCHEM grant 1410557. H.-R. Wenk acknowledges support from National Science Foundation grant EAR-1343908.

## REFERENCES CITED

Abdolhosseini Qomi, M.J., Ulm, F.-J., and Pellenq, R.J.-M. (2012) Evidence on the Dual Nature of Aluminum in the Calcium-Silicate-Hydrates Based on Atomistic Simulations. Journal of the American Ceramic Society 95[3], 1128–1137.

Aguirre, L., Dominguez-Bell, S., Morata, D., and Winke, O. (1998) An occurrence of tobermorite in Tertiary basalts from Patagonia, Chile. Canadian Mineralogist, 36, 1149–1155.

ASTM (2015) Standard specification for coal fly ash and raw or natural pozzolan for use in concrete (C618-12a), ASTM International, West Conshohocken, PA. www.astm.org.

Barnes, M.W., and Scheetz, B.E. (1991) The chemistry of Al-tobermorite and its coexisting phases at 175 °C. In B.E. Scheetz, A.G. Landers, I. Oder, and H. Jennings, Eds., Specialty cements with advanced properties, 179, 243–271. Material Research Society Symposium Proceedings, Warrendale, Pennsylvania.

Behrens, G., Kuhn, L.T., Ubic, R., and Heuer, A.H. (1995) Raman spectra of vateritic calcium carbonate. Spectroscopy Letters, 28[6], 983–995.

Biagioni, C., Merlino, S., and Bonaccorsi, E. (2015) The tobermorite supergroup: A new nomenclature. Mineralogical Magazine, 79[2], 485–495.

Black, L. (2009) Raman spectroscopy of cementitious materials. Spectroscopic Properties Inorganic Organometric Compounds, 40, 72–127.

Black, L., Breen, C., Yarwood, J., Garbev, K., Stemmerman, P., and Gasharova, B. (2007) Structural Features of C–S–H(I) and Its Carbonation in Air—A Raman Spectroscopic Study. Part II: Carbonated Phases. Journal of the American Ceramic Society, 90, 908–917.

599 Brandon, C., Hohlfelder, R.L., Jackson, M.D., and Oleson, J.P. (2014) Building for Eternity:
600 The History and Technology of Roman Concrete Engineering in the Sea. Oxbow Books,
601 Oxford, 327 p.
602 Brune, P.F., Ingraffea, A.R., Jackson, M.D., and Perucchio, R. (2013) The fracture toughness of
603 an Imperial Roman mortar. Engineering Fracture Mechanics, 102, 65–76.
604 Cai, G., Noguchi, T., Degée, H., Zhao, J., and Kitagaki, R. (2016) Environmental Science and
605 Pollution Research, 23, 7220–7243.
606 Celik, K., Jackson, M.D., Mancio, M., Meral, C., Emwas, A.M., Mehta, P.K., and Monteiro,
607 P.J.M. (2014) High-volume natural volcanic pozzolan and limestone powder as partial
608 replacements for Portland cement in self-compacting and sustainable concrete. Cement
609 and Concrete Composites, 45, 136–147.
610 Claringbull, G.F., and Hey, M. (1952) A re-examination of tobermorite. Mineralogical
611 Magazine, 29, 960–962.
612 Coleman, N.J., Li, Q., and Raza, A. (2014) Synthesis, structure and performance of calcium
613 silicate ion exchangers from recycled container glass, Physicochemical Problems in
614 Mineral Processing, 50, 5–16.
615 Deer, W.A., Howie, R.A., Wise, W.S., and Zussman, J. (2004) Rock-forming minerals. Vol. 4B,
616 Framework silicates: silica minerals, feldspathoids and the zeolites, London, Geological
617 Society of London.
618 de Gennaro, M., Cappelletti, P., Langella, A., Perrotta, A., and Scarpati, C. (2000) Genesis of
619 zeolites in the Neapolitan Yellow Tuff: Geological, volcanological and mineralogical
620 evidence. Contributions to Mineralogy and Petrology, 139, 17–35.

de Gennaro, M., Incoronato, A., Mastrolorenzo, G., Adabbo, M., and Spina, G. (1999) Depositional mechanisms and alteration processes in different types of pyroclastic deposits from Campi Flegrei volcanic field (Southern Italy). Journal of Volcanological and Geothermal Research, 91, 303–320.

Damiani, V. Baudo, R. De Rosa, S., De Simone, R., Ferretti, O., Izzo, G., and Serena, F. (1987) A case study: Bay of Pozzuoli (Gulf of Naples, Italy). Hydrobiologia, 149, 201–211.

Fedele, L., Insinga, D.D., Calvert, A.T., Morra, V., Perrotta, A., and Scarpati, C. (2011) 40Ar/39Ar dating of tuff vents in the Campi Flegrei caldera, southern Italy. Bulletin of Volcanology 73, 1323–1336.

Frost, R.L., Tran, T.H., Rintoul, L., and Kristol, J. (1998) Raman microscopy of dickite, kaolinite, and their intercalates. Analyst, 123, 611–616.

Gatta, G.D., Cappelletti, P., and Langella, A. (2010) Crystal chemistry of phillipsites from the Neapolitan Yellow Tuff. European Journal of Mineralogy, 22, 779 –786.

Gaucher, E.C., and Blanc, P. (2006) Cement/clay interactions - A review: Experiments, natural analogues, and modeling. Waste Management 26, 776–788.

Giaramita, M.J., and Day, H.W. (1990) Error propagation in calculations of structural formulas. American Mineralogist, 75, 170–182.

Goñl, S., Lorenzo, M.P., Guerrero, A., and Hernández, M.S. (2005) Calcium hydroxide saturation factors in the pore solution of hydrated portland cement fly ash paste. Journal of the American Ceramic Society, 79[4], 1041–1046.

Gotti, E., Oleson, J. P., Bottalico, L., Brandon, C., Cucitore, R., and Hohlfelder, R.L. (2008) A comparison of the chemical and engineering characteristics of ancient Roman hydraulic concrete with a modern reproduction of Vitruvian hydraulic concrete. Archaeometry, 50,

576–590.

Gualtieri, A.F. (2000) Accuracy of XRPD QPA using the combined Rietveld-RIR method, Locality: Vallerano, Rome, Italy. Journal of Applied Crystallography, 33, 267–278.

Hay, R.L. (1966) Zeolite and zeolite reactions in sedimentary rocks. Geological Society of America Special Paper 85.

Hay, R.L., and Iijima, A. (1968) Nature and origin of palagonite tuffs of the Honolulu group on Oahu, Hawaii. Geological Society of America Memoir, 116, 331–376.

Hay, R.L., and Sheppard, R.A. (2001) Occurrence of zeolites in sedimentary rocks: an overview. Reviews in Mineralogy and Geochemistry, 45, 217–234.

Hazen, R.M., Papineau, D., Bleeker, W., Downs, R.T., Ferry, J.M., McCoy, T.J., Sverjensky, D.A., and Yang, H. (2008) Mineral Evolution. Americn Mineralogist, 93, 1693–1720.

Henmi, C., and Kusachi, I. (1992) Clinotobermorite, $Ca_5Si_6(O, OH)_{18}5H_2O$, a new mineral from Fuka, Okayama Prefecture, Japan. Mineralogical Magazine, 56, 353–358.

Hoffman, C., and Armbruster, T. (1997) Clinotobermorite, $Ca_5[Si_3O_8(OH)]_{24}\,H_2O$, a natural C-S-H(I) type cement mineral: Determination of the substructure. Zeitschrift für Kristallographie, 212, 864–873.

Jackson, M.D. (2014) Seawater Concretes and their Material Characteristics. In J. P. Oleson, Ed., Building for Eternity: the History and Technology of Roman Concrete Engineering in the Sea, p. 141–187, Oxbow Books, Oxford.

Jackson, M.D., Chae, S.R., Mulcahy, S.R., Meral, C., Taylor, R., Li, P., Emwas, A.H., Moon, J., Yoon, S., Vola, G., Wenk, H.-R., and Monteiro, P.J.M. (2013a) Unlocking the secrets of Al-tobermorite in Roman seawater concrete. American Mineralogist, 98, 1669–1687.

666 Jackson, M.D., and Kosso, K. (2013) *Scientia* in republican era stone and concrete masonry. in J.
667 R. Evans, Ed., A Companion to the Archaeology of the Roman Republic, 1st edition, p.
668 268-284, Blackwell Publishing Ltd., New York.
669 Jackson, M.D., Moon, J., Gotti, E., Taylor, R., Chae, S.R., Kunz, M., Emwas, A-H., Meral, C.,
670 Guttman, P., Levitz, P., Wenk, H.-R., and Monteiro, P.J.M. (2013b)
671 Material and elastic properties of Al-tobermorite in ancient Roman seawater concrete.
672 Journal of the American Ceramic Society, 96[8], 2598–2606.
673 Jackson, M.D., Landis, E.N., Brune, P.B., Vitti, M., Chen, H., Li, Q., Kunz, M., Wenk, H.-R.,
674 Monteiro, P.J.M., and Ingraffea, A.R. (2014) Mechanical Resilience and Cementitious
675 Processes in Imperial Roman Architectural Mortar. Proceedings National Academy
676 Sciences, 111, 18485–18489.
677 Jackson, M.D., Vola, G., Všianský, D., Oleson, J.P., Scheetz, B., Brandon, C., and Hohlfelder,
678 R.L. (2012) Cement microstructures and durability in ancient Roman seawater concretes.
679 In J. Valek, C. Groot, J. Hughes, Eds. Historic Mortars, Characteristics and Tests, p. 49–
680 76, Springer – RILEM, Berlin.
681 Jakobsson, S., and Moore, J.G. (1986) Hydrothermal minerals and alteration rates at Surtsey
682 volcano, Iceland. Geological Society of America Bulletin, 97, 648–659.
683 Jantzen, C.M., Crawford, C.L., Trivelpiece, C., Pareizs, J.M., and Picket, J.B. (in press)
684 Accelerated Leach Testing of GLASS (ALTGLASS): II. Mineralization of Hydrogels by
685 Leachate Strong Bases. International Journal of Applied Glass Science (SRNL-STI-2014-
686 00381).
687 Komarneni, S., and Roy, D. (1983) Tobermorites: A new family of cation exchangers. Science,
688 221, 647-648.

689 Komarneni, S., Breval, E., Miyake, M., and Roy, R. (1987) Cation exchange properties of
690 (Al+Na)-substitutes synthetic tobermorites . Clays and Clay Minerals, 35, 385–390.
691 Kirkpatrick, R.J., Yarger, J.L., McMillan, P.F., Yu, P., and Cong, X. (1997) Raman spectroscopy
692 of C-S-H, tobermorite, and jennite. Advances in Cement Based Materials, 5, 93–99.
693 Lalan, P., Dauzères, A., DeWindt, L., Bartier, D., Sammaljärvi, J., Barnichon, J.-D., Techer, I.,
694 and Detilleux, V. (2016) Impact of a 70 °C temperature on an ordinary Portland cement
695 paste/claystone interface: An in situ experiment. Cement and Concrete Research, 83,
696 164–178.
697 L'Hôpital, E.L., Lothenbach, B., Scrivener, K., and Kulik, D.A. (2016) Alkali uptake in calcium
698 alumina silicate hydrate (C-A-S-H). Cement and Concrete Research, 85, 122–136.
699 Livingstone, A. (1988) Reyerite, tobermorite, calcian analcime and bytownite from amygdules in
700 Skye basalt. Mineralogical Magazine, 52, 711–713.
701 Lothenbach, B., Scrivener, K., and Hooton, R.D. (2011) Supplementary cementitious materials.
702 Cement and Concrete Research, 41, 217–229.
703 Marra, F., Jackson, M.D., Deocampo, D., and Ventura, G. (2009) Large mafic eruptions at Alban
704 Hills Volcanic District (Central Italy). Journal of Volcanic and Geothermal Research,
705 179, 217–232.
706 Massazza, F. (1985) Concrete resistance to seawater and marine environment. Il Cemento, 82,
707 26–85.
708 Massazza, F. (2004) Pozzolana and pozzolanic cements. In P. C. Hewlett, P.C., Lea's Chemistry
709 of Cement and Concrete, 4th edition, p. 471–602, Elsevier, Oxford.
710 Matter, J.M., Stute, M., Snæbjörnsdottir, S., Ó. Oelkers, E. H., Gislason, S. R., Aradottir, E.S.,
711 Sigfusson, B., Gunnarsson, I., Sigurdardottir, H., Gunnlaugsson, E., Axelsson, G.,

712 Alfredsson, H.A., Wolff-Boenisch, D., Mesfin, K., Fernandez de la Reguera Taya, D.,
713 Hall, J., Dideriksen, K., and Broecker, W.S. (2016) Rapid carbon mineralization for
714 permanent disposal of anthropogenic carbon dioxide emissions. Science, 352, 1312–
715 1314.
716 McMillan, P., and Piriou, B. (1982) The structures and vibrational spectra of crystals and glasses
717 in the silica-alumina system. Journal of Non-Crystalline Solids, 53, 279–298.
718 McMillan, P., Piriou, B., and Navrotsky, A. (1982) A Raman spectroscopic study of glasses
719 along the joins silica-calcium aluminate, silica-sodium aluminate, and silica-potassium
720 aluminate. Geochimica and Cosmochimica Acta, 46, 2021–2037.
721 Mehta, P.K. (1987) Natural Pozzolans: Supplementary cementing materials for concrete.
722 CANMET Special Publication, 86, 1–33.
723 Mehta, P.K. (1990) Concrete in the Marine Environment. Elsevier, Oxford.
724 Mehta, P., and Monteiro, P.J.M. (2015) Concrete: Microstructure, Properties, and Materials. 4th
725 Edition. McGraw Hill, New York.
726 Meier, D.C., Davis, J.M., and Vicenzi, E.P. (2011) An examination of kernite
727 ($Na_2B_4O_6(OH)_2 \cdot 3H_2O$) using x-ray and electron spectroscopies: Quantitative microanalysis
728 of a hydrated low-Z mineral. Microscopy and Microanalysis, 17, 718–727.
729 Mertens, G., Snellings, R., Van Balen, K., Bicer-Simsir, B., Verlooy, P., and Elsen, J. (2009)
730 Pozzolanic reactions of common natural zeolites with lime and factors affecting their
731 reactivity. Cement and Concrete Research, 39, 233–240.
732 Merlino, S., Bonaccorsi, E., and Armbruster, T. (2001) The real structure of 11Å tobermorite:
733 normal and anomalous forms, OD character and polytypic modifications. European
734 Journal of Mineralogy, 13, 577–590.

735 Mitsuda, T., and Taylor, H.F.W. (1978) Normal and anomalous tobermorites. Mineralogical
736 Magazine, 42, 229–235.
737 Myers, R.P., L'Hôpital, E., Provis, J.L., and Lothenbach, B. (2015a) Effect of temperature and
738 aluminium on calcium (alumino)silicate hydrate chemistry under equilibrium conditions.
739 Cement and Concrete Research, 68, 83–93.
740 Myers, R.P., L'Hôpital, E., Provis, J.L., and Lothenbach, B. (2015b) Composition–solubility–
741 structure relationships in calcium (alkali) aluminosilicate hydrate (C-(N, K-)A-S-H).
742 Dalton Transactions, DOI: 10.1039/c5dt01124h.
743 Oleson, J.P. (2014) Ancient literary sources concerned with Roman concrete technology. In J. P.
744 Oleson, Ed., Building for Eternity, p. 11–36, Oxbow Books, Oxford.
745 Oleson, J.P., Bottalico, L., Brandon, C, Cucitore, R., Gotti E., and Hohlfelder R.L. (2006),
746 Reproducing a Roman maritime concrete structure with Vitruvian pozzolanic concrete.
747 Journal of Roman Archaeology, 19, 29–52.
748 Passaglia, E., Vezzalini, G., and Carnevali, R. (1990) Diagenetic chabazites and phillipsites in
749 Italy: crystal chemistry and genesis. European Journal of Mineralogy, 2, 827–839.
750 Provis, J.L., and Bernal, S.A. (2014) Geopolymers and related alkali-activated construction
751 materials. Annual Reviews of Material Research, 44, 299–327.
752 Richardson, I.G. (2014) Model structures for C-(A)-S-H(I). Acta Crystallographica, B70, 903–
753 923.
754 Richardson, I.G., Skibsted, J., Black, L., and Kirkpatrick, R.L. (2010) Characterisation of cement
755 hydrate phases by TEM, NMR and Raman spectroscopy. Advances in Cement Research,
756 22, 233–248.
757 Sharma, S.K., Simons, B., and Yoder, H.S. (1982) Raman study of anorthite, calcium

Tschermak's pyroxene, and gehlenite in crystalline and glassy states. American Mineralogist, 68, 1113–1125.

Sheppard, R.A., and Hay, R.L. (2001) Formation of zeolites in open hydrologic systems. Reviews in Mineralogy and Geochemistry, 45, 261–276.

Stanislao, C., Rispoli, C., Vola, G., Cappelletti, P., Morra, V., and de Gennaro, M. (2011) Contribution to the Knowledge of Ancient Roman Seawater Concretes. Phlegrean Pozzolan Adopted in the Construction of the Harbour at Soli-Pompeiopolis (Mersin, Turkey). Periodico di Mineralogia, 80, 471–488.

Snellings, R. (2015) Surface chemistry of calcium aluminosilicate glasses. Journal of the American Ceramic Society, 98[1], 303–314.

Snellings, R., Mertens, G., and Elsen, J. (2012) Supplemental cementitious materials. Reviews Mineralogy Geochemistry, 74, 211–278.

Tamura, N., Kunz, M., Chen, K., Celestre, R.S., MacDowell, A.A., and Warwick, T. (2009) A Superbend X-Ray Microdiffraction Beamline at the Advanced Light Source. Material Science and Engineering A, 524, 28.

Taylor, H.F.W. (1992) Tobermorite, jennite, and cement gel. Zeitschrift für Kristallographie, 202, 41–50.

Taylor, M.W., and Surdam, R.C. (1981) Zeolite reactions in the tuffaceous sediments at Teels March, Nevada. Clays and Clay Minerals, 29[5], 314–352.

Trotignon, L., Devallois, V., Peycelon, H., Tiffreau, C., and Bourbon, X. (2007) Predicting the Long Term Durability of Concrete Engineered Barriers in a Geological Repository for Radioactive Waste. Physics and Chemistry of the Earth, Parts A/B/C, 32 [1–7] 259–74.

780 Tsuji, M., and Komarneni, S. (1989) Alkali metal ion exchange selectivity of Al-substituted
781 tobermorite. Journal of Material Research, 4, 698–703.
782 Vanorio, T., and Kanitpanyacharoen, W. (2015) Rock physics of fibrous rocks akin to Roman
783 concrete explains uplifts at Campi Flegrei caldera. Science, 349, 617–621.
784 Yamazaki, S., and Toraya, H. (2001) Determination of positions of zeolitic calcium atoms and
785 water molecules in hydrothermally formed aluminum-substituted tobermorite-1.1 nm
786 using synchrotron radiation. Journal of the American Ceramic Society, 84, 2685–2690.
787 Youssef, H., Ibrahim, D., Komarneni, S., and Mackenzie, K.J.D. (2010) Synthesis of 11Å Al-
788 substituted tobermorite from trachyte rock by hydrothermal treatment. Ceramics
789 International, 36, 203–209.
790 Wehrmeister, U., Soldati, A.L., Jacob, D.E., Häger, T., and Hofmeister, W. (2010) Raman
791 spectroscopy of synthetic, geological and biological vaterite a Raman spectroscopic
792 study. Journal of Raman Spectroscopy, 41, 193–201.

793 **FIGURE CAPTIONS**

794 **Figure 1.** Authigenic mineral textures in tuff deposits and Roman marine mortar. Scanning
795 electron microscopy backscattered electron (SEM-BSE) images. a, *Portus Cosanus* pier,
796 Orbetello, Italy (credit, J. P. Oleson) (Fig. 2). b, Bacoli tuff (BT), pumice clast. c, d, Neapolitan
797 Yellow Tuff (NYT), dissolving alkali feldspar, phillipsite and chabazite textures. e, Surtsey tuff,
798 Iceland, 1979 drill core, dissolving phillipsite and associated Al-tobermorite, 37.0 m, 100 °C
799 (credit, J. G. Moore). f, *Portus Cosanus*, pumice clast with dissolved glass. g, *Portus Neronis*,
800 Anzio, Italy, dissolving alkali feldspar (see also Fig. 5). h, *Portus Cosanus*, phillipsite textures. i,
801 *Portus Cosanus*, dissolving Campi Flegrei phillipsite [1], pozzolanic C-A-S-H binder [2] and Al-

802 tobermorite [3] (see Fig. 7i for X-ray microdiffraction patterns). j, *Portus Baianus*, Pozzuoli,
803 Italy, dissolving *in situ* phillipsite and associated Al-tobermorite (Fig. 9).
804 **Figure 2**. Ancient Roman concrete harbors and ROMACONS project drill sites, green circles: 1
805 *Portus Cosanus*, 2 *Portus Traianus*, 3 *Portus Neronis*, 4 *Baianus Sinus*. Volcanic districts, red
806 triangles (after Jackson et al. 2013a).
807 **Figure 3.** Compositions of phillipsite and Al-tobermorite in Roman marine mortars and geologic
808 deposits. Electron probe microanalyses (EPMA), as molecular proportions (Tables 1, 2, S1). a,
809 Phillipsite, published compositions from [1] Passaglia et al. 1990; [2] de Gennaro et al. 2000; [3]
810 Gatta et al. 2010; [4] Jakobsson and Moore 1986. b, Al-tobermorite, various geologic deposits
811 (after [5] Jackson et al. 2013a). [6] Aguirre et al. 1998, Claringbull and Hey 1952; [7]
812 Livingstone 1988; [8] Henmi and Kusachi 1992; [9, 10] Hoffman and Armbuster 1997; Merlino
813 et al. 2001; [11] Mitsuda and Taylor 1978. Roman crystals have Al/(Si+Al) = 0.10–0.16 and
814 Ca/(Si+Al) = 0.45–0.69. Sodium and potassium range from 1–3 weight%. ANZ, *Portus Neronis*;
815 BAI, *Baianus Sinus*; PCO, *Portus Cosanus*; NYT, Neapolitan Yellow Tuff; BT, Bacoli Tuff.
816 **Figure 4.** Compositions of phillipsite and Al-tobermorite in Roman marine mortars and geologic
817 deposits. Electron probe microanalyses (EPMA), as molecular proportions (Tables 1, 2, S1). a,
818 Phillipsite, Ca+Mg-Na-K, see Fig. 2 for references to published compositions. Phillipsite
819 compositions in relict voids of *Portus Traianus* mortar, Ostia, Italy, are similar to phillipsite in
820 Tufo Lionato (TL) tuff coarse aggregate, erupted at 366±5 ka from Alban Hills volcano (Marra
821 et al. 2009). b, Al-tobermorite, Si-Ca-Na+K, various geologic deposits (after [5] Jackson et al.
822 2013a). The most silicic compositions are similar to Al-tobermorite in Surtsey basaltic tuff,
823 Iceland (Jakobsson and Moore 1986). Tobermorite is not observed in NYT, BT, and TL, but
824 occurs in deeper Campi Flegrei deposits (Vanorio and Kanitpanyacharoen 2015).

825 **Figure 5**. Dissolution in *Portus Neronis* mortar and associated crystalline cementitious phases,
826 strätlingite and Al-tobermorite in the interfacial perimeter. a, *In situ* dissolution of a alkali
827 feldspar crystal fragment produced a 100 $\mu m^2$ dissolution mold in the already hardened
828 cementing matrix, petrographic image. b, X-ray diffraction patterns for cementitious minerals in
829 the interfacial zone of the partially dissolved alkali feldspar single crystal (F) determined through
830 X-ray microdiffraction include strätlingite (S), Al-tobermorite (T), and calcite (C), only weak
831 reflections of the feldspar single crystal are shown by the monochromatic X-ray beam; q is
832 calculated as $2\pi$/d-spacing.
833 **Figure 6.** Images of Al-tobermorite and zeolite in pumice clasts. a, Portus Cosanus, *Portus*
834 *Cosanus*, dissolving Campi Flegrei phillipsite [1], pozzolanic C-A-S-H binder [2] and Al-
835 tobermorite [3], and later accumulations of very fine grained Al-tobermorite [4]. b, *Portus*
836 *Neronis*, examples of EPMA analyses in *Portus Neronis* mortar pumice clasts, with partially
837 dissolved alkali feldspar, relict geologic phillipsite, and associated Al-tobermorite in vesicles.
838 **Figure 7.** Comparison of microstructures showing Al-tobermorite crystallization in association
839 with zeolite alteration. a–h, *Portus Cosanus*, pumice clast. j–o, *Baianus Sinus*, relict pores in the
840 cementing matrix. SEM BSE images, energy dispersive X-ray (SEM-EDS) spectroscopy maps
841 and X-ray microdiffraction maps (see Figs. 8, 9 for details). i, X-ray microdiffraction patterns,
842 *Portus Cosanus* pumice clast: early Al-tobermorite (*A*, Fig. 1j, location [1]), later Al-tobermorite
843 (*B*, Fig. 1j, in vesicle near [1], *C*, Fig. 8b, location #66) and strätlingite (*D*, Fig. 8d, location #06).
844 Reference Al-tobermorite diffraction patterns from [1] Jackson et al. 2013a, *Baianus Sinus* relict
845 lime clast, [2] Yamazaki and Toraya 2001, Al-tobermorite synthesis; SEM-EDS maps b, c, f, g
846 scaled to red=20 normalized mass% at each point; SEM-EDS maps l–p scaled to red=maximum
847 mass %: Al, 9.5; Si, 24.7; K, 6.7; Na, 18.6; S, 10.2; Cl, 3.7.

848 **Figure 8**. Authigenic Al-tobermorite and strätlingite associated with geologic phillipsite and
849 chabazite and *in situ* vaterite and calcite in a *Portus Cosanus* pumice clast (Fig. 7a–i). a, c, SEM-
850 BSE images. Note rounded perimeters of phillipsite rosettes (a) and carbonation of chabazite to
851 form calcite (c). b, d, X-ray microdiffraction maps, phillipsite (Phi), Chabazite (Cbz), and *in situ*
852 Al-tobermorite (Al-tbm), Strätlingite (Strat), Vaterite (Vtr), Calcite (Cal), and an amorphous
853 calcium carbonate phase. Asterisk (*) represents spotty Debye ring patterns indicative of crystals
854 too coarse (> 3 μm) to produce regular diffraction rings with the monochromatic X-ray beam.
855 Fig. 7i analyses: (b) Al-tobermorite (*C*), #66, with strong vaterite pattern; (d) strätlingite (*D*),
856 #06, with weak vaterite pattern.
857 **Figure 9**. Authigenic mineral syntheses in relict voids of the cementing matrix, submarine
858 *Baianus Sinus* mortar (Fig. 7j–n). a, b, SEM-BSE images showing relict pores with *in situ*
859 crystalline textures. c, Diffraction patterns for Roman phillipsite and Al-tobermorite in (d) and
860 phillipsite in a *Baianus Sinus* pumice vesicle compared with Campi Flegrei (Gatta et al. 2010)
861 and Alban Hills phillipsite (Gualtieri et al. 2000). d, X-ray microdiffraction map, including Fig.
862 7n, showing *in situ* phillipsite (Phi), Al-tobermorite (Al-tbm), Ettringite (Ett), Vaterite (Vtr),
863 Calcite (Cal), Unknown (U). Asterisk (*) represents spotty Debye ring patterns indicative of
864 crystals too coarse (> 3 μm) to produce regular diffraction rings with the monochromatic X-ray
865 beam. Fig. 10 X-ray diffraction patterns for Al-tobermorite at sites (**6**) BAIZ_63, and (**7**)
866 BAIZ_15 (Fig. 8d, #63 and #15), and Raman spectra for Al-tobermorite at sites (**6**) BAIZ_19, (**7**)
867 BAIZ_17 (Fig. 9d, near #59). e, SEM-EDS maps, silicon (Si), aluminum (Al), sodium (Na) and
868 sulfur (S) concentrations normalized to 20 mass% (red).
869 **Figure 10.** X-ray microdiffraction patterns and Raman spectra for Al-tobermorite in diverse
870 microstructural environments in *Baianus Sinus* mortar: relict lime clasts, pumice clasts and relict

voids. a, Al-tobermorite X-ray microdiffraction patterns from relict lime clasts, sites (**1**) LLP_24, (**2**) SPH3_28, (**3**) PM_L233; pumice clasts, sites (**4**) PM_P19, (**5**) PM_17; relict voids: sites (**6**) BAIZ_63, (**7**) BAIZ_15 (see Fig. 9d, #63, #15). b, Al-tobermorite Raman spectra from the same or nearby crystals in the same microstructures: relict lime clasts: sites (**1**) LLP_15, (**2**) SPH3_29, (**3**) PL_1; pumice clasts, sites (**4**) PL_4, (**5**) PL_5; relict voids: sites (**6**) BAIZ_19, (**7**) BAIZ_17 (see Fig. 9d, near #59). Raman spectra for calcite and vaterite (Behrens et al. 1995, Wehermeister et al. 2010).

**Figure 11.** Raman spectra of *Baianus Sinus* C-A-S-H binder and Al-tobermorite, compared with calcium-silicate-hydrate (C-S-H) binder and ideal tobermorite. Inferred $Q^3$ linkages are shown in italics. Published compositions from [1] Kirkpatrick et al. 1997; [2] http://rruff.info/Tobermorite R060147). Bands at 1074 and 1086 indicate C–O stretching in calcite (C) and vaterite (V).

**Figure 12.** $^{29}$Si Nuclear magnetic resonance (NMR) of Al-tobermorite in *Baianus Sinus* relict lime clasts (after Jackson et al. 2013b).

## TABLES

**Table 1.** Phillipsite compositions measured by EPMA. Formulas were calculated on the basis of 16 oxygen and H2O by stoichiometry. Uncertainties in the weight percent oxides were determined from the counting statistics and propagated through the calculation to the number of formula units (Giaramita and Day 1990).

**Table 2**. Al-tobermorite compositions measured by EPMA. Formulas calculated on the basis of 18[O, (OH) and total $H_2O$ was calculated by stoichiometry. Uncertainties in the weight percent oxides were determined from the counting statistics and propagated through the calculation to the number of formula units (Giaramita and Day 1990).

893 **Table 3**. Assignments of Raman frequency shifts to silicate and aluminate linkages in *Baianus*
894 *Sinus* C-A-S-H and Al-tobermorite compared with previous studies of C-S-H and tobermorite.
895 **Table A1**. Roman texts describing the geologic materials and cementitious processes of marine
896 concrete (Oleson 2014). Increasing complexity in Roman construction durability and
897 architectural design through invention, technology transfer, and competitive selection is
898 described explicitly by Vitruvius in *de Architectura* (2.1.2, 2.1.7). Historical intervals of
899 accelerated late Republican era innovations in construction engineering produced the resilient
900 and rock-like Roman harbor concrete structures (Jackson and Kosso 2013; Brandon et al. 2014).
901 **Table S1.** Phillipsite compositions measured by EPMA. Formulas were calculated on the basis
902 of 16 oxygen and $H_2O$ by stoichiometry. Uncertainties in the weight percent oxides were
903 determined from the counting statistics and propagated through the calculation to the number of
904 formula units following (Giaramita and Day 1990).
905
906
907

Figure 1

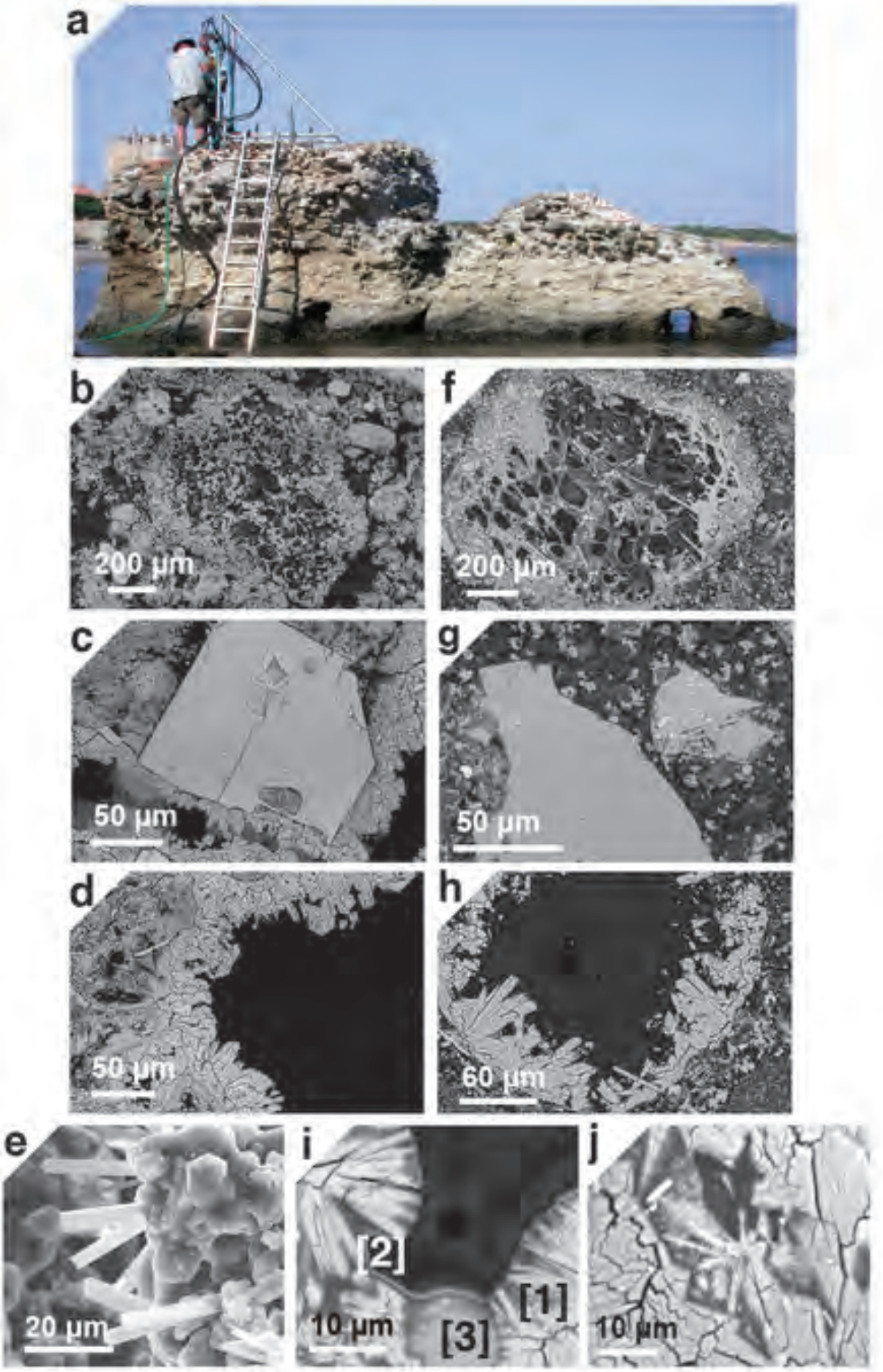
a
b
200 µm
f
200 µm
c
50 µm
g
50 µm
d
50 µm
h
60 µm
e
20 µm
i
[2]
[1]
10 µm
[3]
j
10 µm


N
Italy
Orbetello
Vulsini
Monti Sabatini
Corsica
Alban Hills
Rome
Ostia
Anzio
Naples
Campi Flegrei
Vesuvius
Sardinia
Mediterranean Sea
Sicily
1
2
3
4
0 100 200 km
45.13°N, 6.42°E
37.01°N, 6.42°E
40.12°N, 18.92°E
36.36°N,15.01°E

Figure 3

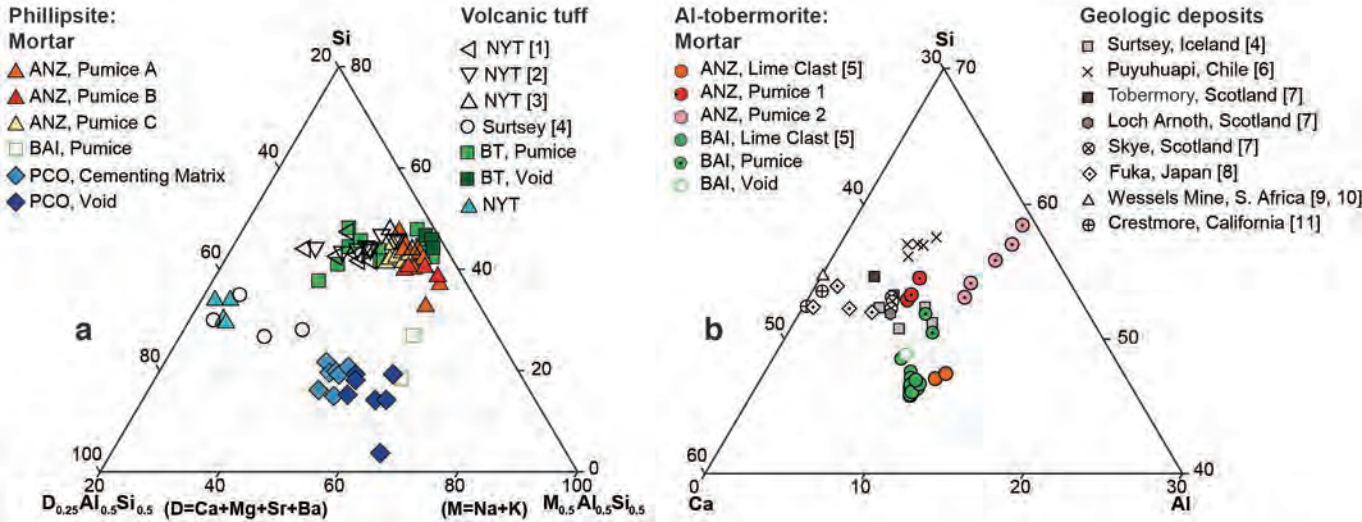
Phillipsite:
Mortar
ANZ, Pumice A
ANZ, Pumice B
ANZ, Pumice C
BAI, Pumice
PCO, Cementing Matrix
PCO, Void
Volcanic tuff
NYT [1]
NYT [2]
NYT [3]
Surtsey [4]
BT, Pumice
BT, Void
NYT
Si
a
$D_{0.25}Al_{0.5}Si_{0.5}$ (D=Ca+Mg+Sr+Ba)
(M=Na+K) $M_{0.5}Al_{0.5}Si_{0.5}$
Al-tobermorite:
Mortar
ANZ, Lime Clast [5]
ANZ, Pumice 1
ANZ, Pumice 2
BAI, Lime Clast [5]
BAI, Pumice
BAI, Void
Geologic deposits
Surtsey, Iceland [4]
Puyuhuapi, Chile [6]
Tobermory, Scotland [7]
Loch Arnoth, Scotland [7]
Skye, Scotland [7]
Fuka, Japan [8]
Wessels Mine, S. Africa [9, 10]
Crestmore, California [11]
b
Ca
Al

Figure 4

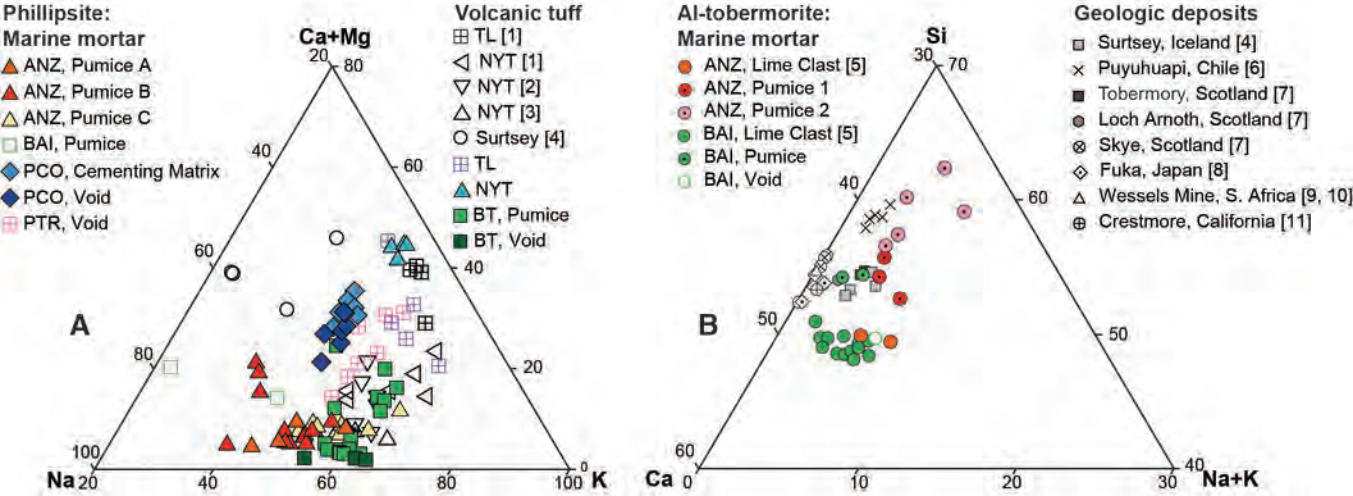
Phillipsite:
Marine mortar
ANZ, Pumice A
ANZ, Pumice B
ANZ, Pumice C
BAI, Pumice
PCO, Cementing Matrix
PCO, Void
PTR, Void
Volcanic tuff
TL [1]
NYT [1]
NYT [2]
NYT [3]
Surtsey [4]
TL
NYT
BT, Pumice
BT, Void
Ca+Mg
Na
K
A
Al-tobermorite:
Marine mortar
ANZ, Lime Clast [5]
ANZ, Pumice 1
ANZ, Pumice 2
BAI, Lime Clast [5]
BAI, Pumice
BAI, Void
Geologic deposits
Surtsey, Iceland [4]
Puyuhuapi, Chile [6]
Tobermory, Scotland [7]
Loch Arnoth, Scotland [7]
Skye, Scotland [7]
Fuka, Japan [8]
Wessels Mine, S. Africa [9, 10]
Crestmore, California [11]
Si
Ca
Na+K
B

Figure 5

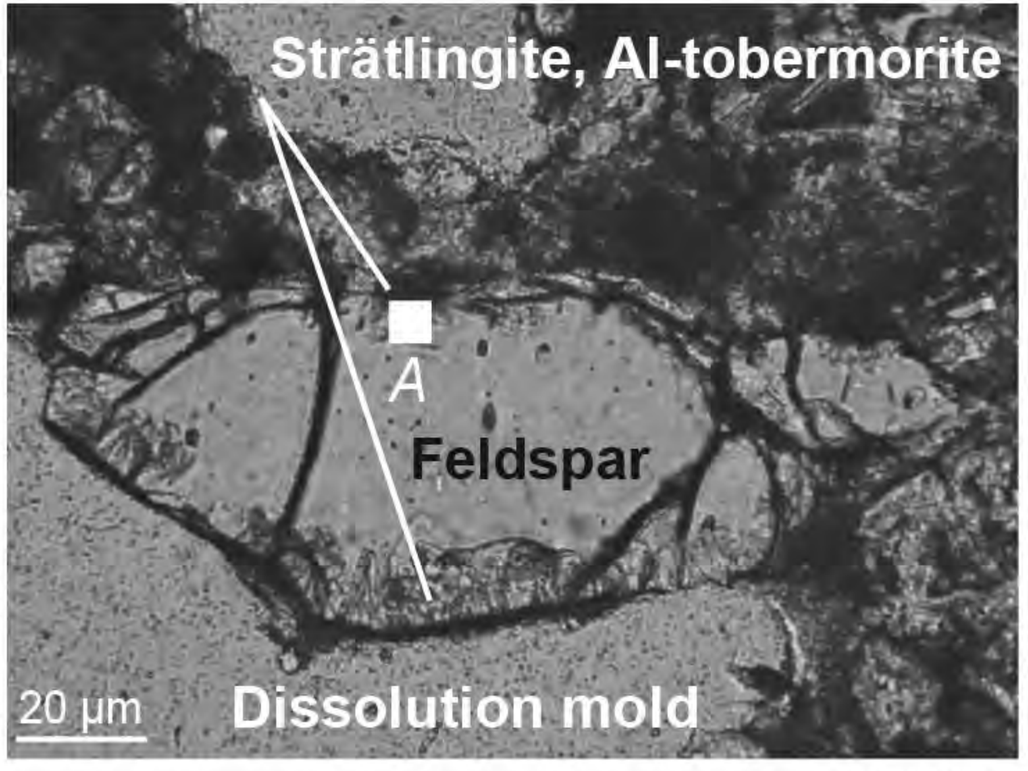


Calcite (**C**)
Strätlingite (**S**)
Al-tobermorite (**T**)
Alkali feldspar crystal fragment (**F**)

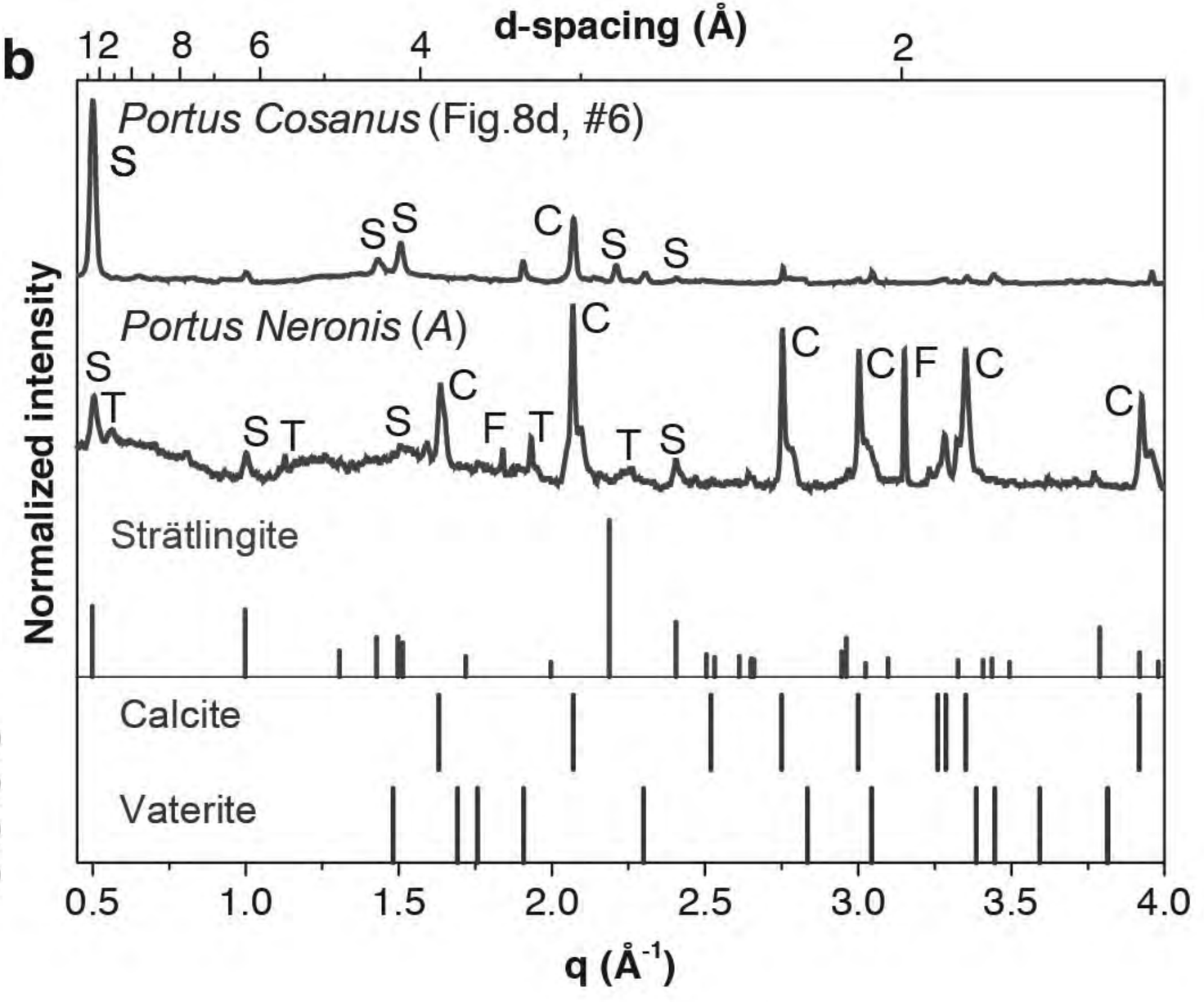

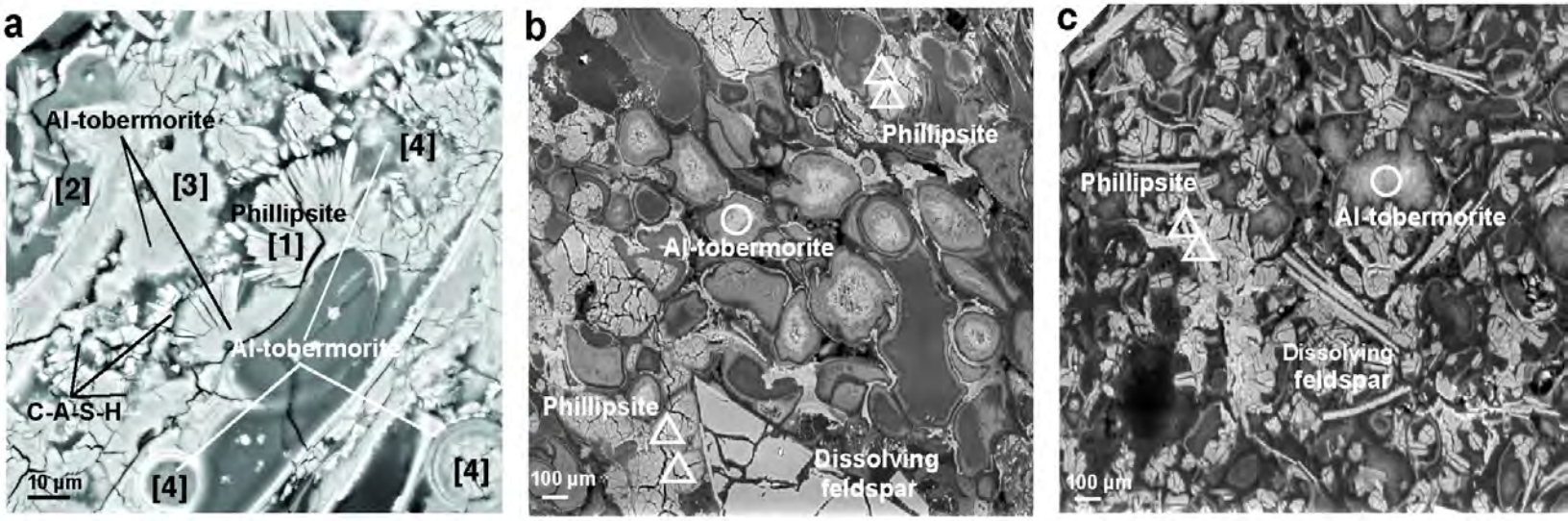
a
Al-tobermorite
[2]
[3]
[4]
Phillipsite
[1]
Al-tobermorite
C-A-S-H
10 µm
[4]
[4]
b
Phillipsite
Al-tobermorite
Phillipsite
Dissolving
feldspar
100 µm
c
Phillipsite
Al-tobermorite
Dissolving
feldspar
100 µm

Figure 7

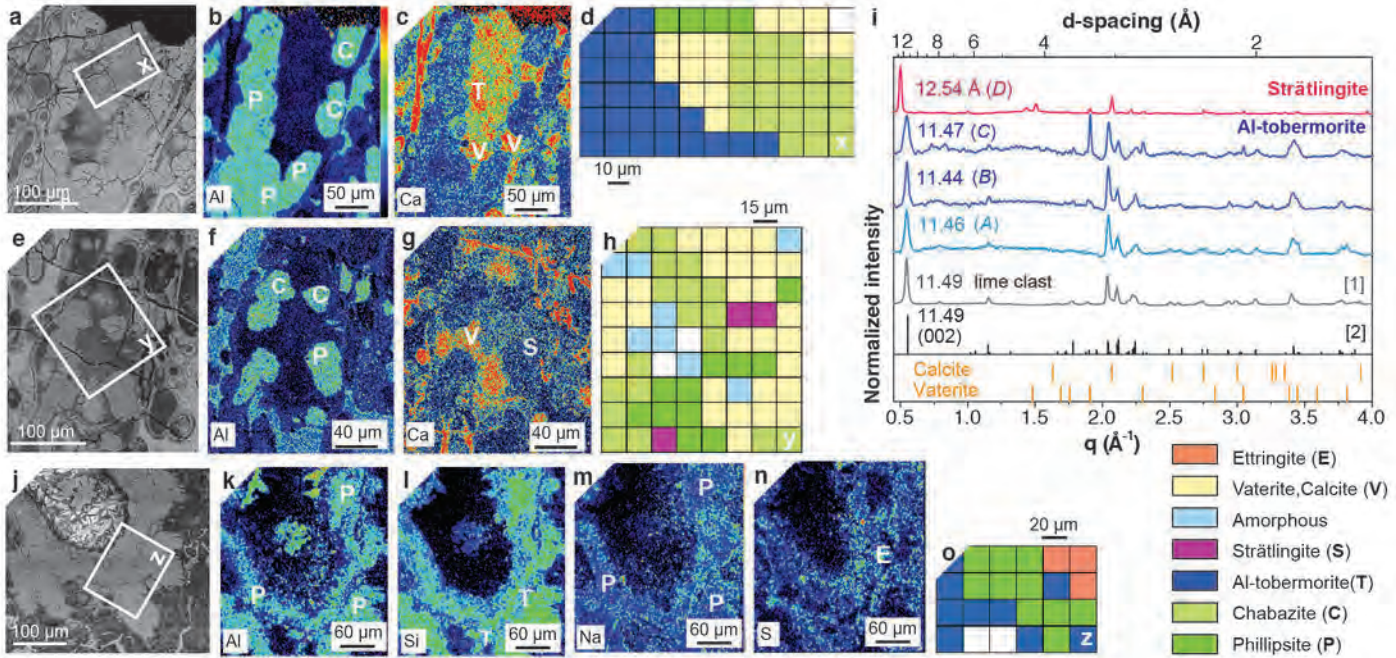
a
X
100 µm
b
C
P
C
P
P
Al
50 µm
c
T
V
V
Ca
50 µm
d
10 µm
x
i
d-spacing (Å)
12
8
6
4
2
12.54 Å (D)
Strätlingite
11.47 (C)
Al-tobermorite
11.44 (B)
11.46 (A)
11.49 lime clast
[1]
11.49
(002)
[2]
Calcite
Vaterite
Normalized intensity
0.5
1.0
1.5
2.0
2.5
3.0
3.5
4.0
q (Å-1)
e
Y
100 µm
f
C
C
P
Al
40 µm
g
V
S
Ca
40 µm
h
15 µm
y
j
Z
100 µm
k
P
P
P
Al
60 µm
l
T
T
Si
60 µm
m
P
P
P
Na
60 µm
n
E
S
60 µm
o
20 µm
z
Ettringite (E)
Vaterite,Calcite (V)
Amorphous
Strätlingite (S)
Al-tobermorite(T)
Chabazite (C)
Phillipsite (P)

Figure 8

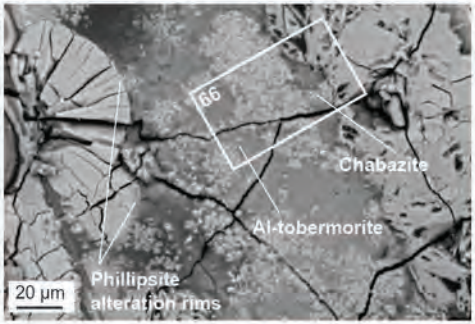


b

| 66 | 65 | 64 | 63 | 62 | 61 | 60 | 59 | 58 | 57 | 56 |
|---|---|---|---|---|---|---|---|---|---|---|
| Al-Tbm Vtr | Al-Tbm Vtr | Al-Tbm Vtr | Phi | Phi | Phi | Phi | Vtr | Vtr | Vtr* | — |
| 55 | 54 | 53 | 52 | 51 | 50 | 49 | 48 | 47 | 46 | 45 |
| Al-Tbm Vtr | Al-Tbm Vtr | Al-Tbm Vtr | Vtr | Vtr Phi | Vtr Phi | Cbz* | Cbz* | Cbz* | Vtr* Calc | Calc |
| 44 | 43 | 42 | 41 | 40 | 39 | 38 | 37 | 36 | 35 | 34 |
| Al-Tbm Vtr | Al-Tbm Vtr | Al-Tbm Vtr | Vtr | Vtr | Vtr | Cbz* | Cbz* | Cbz* | Cbz* | Cbz* |
| 33 | 32 | 31 | 30 | 29 | 28 | 27 | 26 | 25 | 24 | 23 |
| Al-Tbm Vtr | Al-Tbm Vtr | Al-Tbm Vtr | Al-Tbm Vtr | Vtr | Vtr | Cbz* | Cbz* | Cbz* | Cbz* | Cbz* |
| 22 | 21 | 20 | 19 | 18 | 17 | 16 | 15 | 14 | 13 | 12 |
| Al-Tbm Vtr | Al-Tbm Vtr | Al-Tbm Vtr | Al-Tbm Vtr | Al-Tbm Vtr | Vtr | Cbz* | Cbz* | Cbz* | Cbz* | Cbz* |
| 11 | 10 | 9 | 8 | 7 | 6 | 5 | 4 | 3 | 2 | 1 |
| Al-Tbm Vtr | Al-Tbm Vtr | Al-Tbm Vtr | Al-Tbm Vtr | Al-Tbm Vtr | Al-Tbm Vtr | Al-Tbm Vtr | Al-Tbm Cbz* | Cbz* | Cbz* | Cbz* |

10 µm

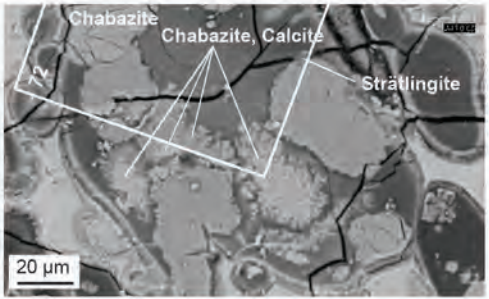


d

| 72 | 71 | 70 | 69 | 68 | 67 | 66 | 65 |
|---|---|---|---|---|---|---|---|
| Vtr | Cbz Vtr* | Cbz | Vtr* | Vtr | Vtr | Vtr Phi | Amorph |
| 64 | 63 | 62 | 61 | 60 | 59 | 58 | 57 |
| Amorph Vtr | Amorph Vtr | Cbz* Calc* | Cbz* | Vtr Calc | Vtr* Calc | Vtr | Calc |
| 56 | 55 | 54 | 53 | 52 | 51 | 50 | 49 |
| Vtr | Vtr | Cbz* | Cbz* | Cbz* Calc | Calc Cbz* | Calc | Phi Calc |
| 48 | 47 | 46 | 45 | 44 | 43 | 42 | 41 |
| Vtr Cbz | Vtr Calc | Amorph | Cbz* | Cbz* | Strat* Calc | Strat* Cbz | Arag |
| 40 | 39 | 38 | 37 | 36 | 35 | 34 | 33 |
| Vtr | Amorph | Amorph | — | Cbz* | Calc | Calc Cbz* | Calc |
| 32 | 31 | 30 | 29 | 28 | 27 | 26 | 25 |
| Vtr | Cbz* Vtr | — | Amorph | Phi | Phi Vtr | Phi | Calc Phi |
| 24 | 23 | 22 | 21 | 20 | 19 | 18 | 17 |
| Cbz* | Cbz* | Phi | Phi | Vtr | Amorph Vtr | Vtr | Calc |
| 16 | 15 | 14 | 13 | 12 | 11 | 10 | 9 |
| Cbz* Calc | Phi Cbz* | Phi Cbz* | Phi Vtr* | Vtr | Vtr | Vtr | Vtr U |
| 8 | 7 | 6 | 5 | 4 | 3 | 2 | 1 |
| Cbz* Calc | Cbz* Calc | Strat* Vtr* | Phi Calc, Vtr* | Phi | Vtr | Cbz* | Cbz |

15 µm

Figure 9

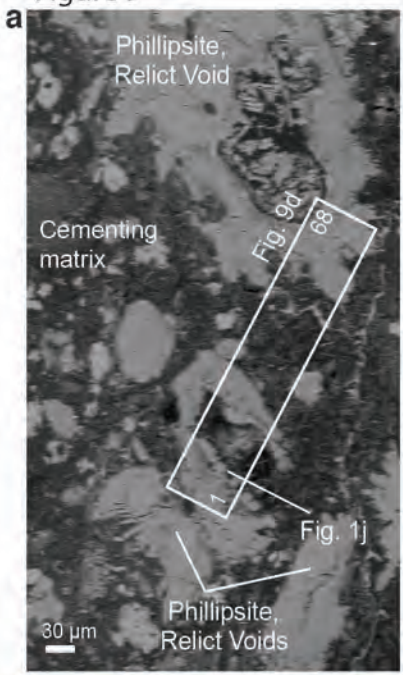


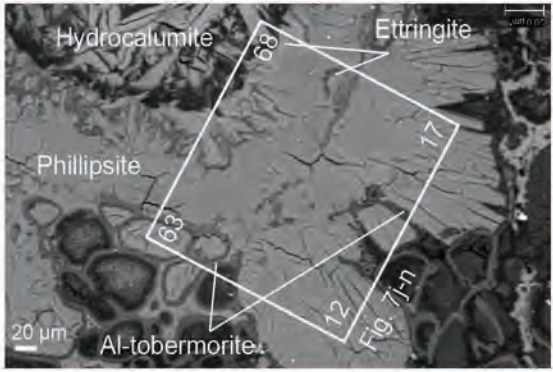


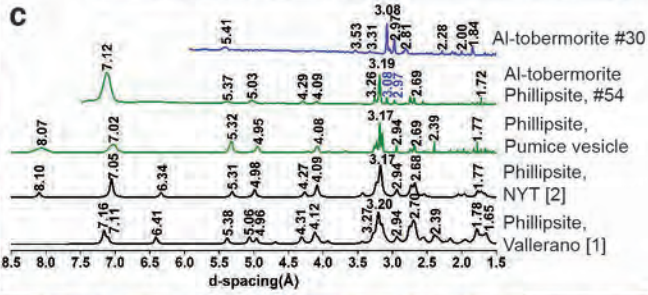


d

| 52 | 53 | 54 | 55 | 56 | 57 | 58 | 59 | 60 | 61 | 62 | 63 | 64 | 65 | 66 | 67 | 68 |
|---|---|---|---|---|---|---|---|---|---|---|---|---|---|---|---|---|
| Al-Tbm | Phi | Phi Al-Tbm | — | — | Phi* Al-Tbm | Phi* | Al-Tbm | Phi* | — | — | Al-Tbm | Phi* | Phi | Phi | Ett U | Ett U |
| 35 | 36 | 37 | 38 | 39 | 40 | 41 | 42 | 43 | 44 | 45 | 46 | 47 | 48 | 49 | 50 | 51 |
| Phi* | Phi | Phi | Phi* | Phi* | Phi* | Phi* | Phi* | Vtr | Vtr | — | Al-Tbm | Phi* | Phi | Phi | Al-Tbm U | Ett U |
| 18 | 19 | 20 | 21 | 22 | 23 | 24 | 25 | 26 | 27 | 28 | 29 | 30 | 31 | 32 | 33 | 34 |
| Phi* | Phi | Phi | Phi* | Phi* | U | Phi* | — | Vtr Al-Tbm | Vtr | — | Al-Tbm | Al-Tbm | Al-Tbm | Phi | Phi | Phi |
| 1 | 2 | 3 | 4 | 5 | 6 | 7 | 8 | 9 | 10 | 11 | 12 | 13 | 14 | 15 | 16 | 17 |
| Phi* | Phi* | Phi* | Phi* | — | U | — | — | — | — | Vtr | Al-Tbm | — | U | Al-Tbm | Phi* | Al-Tbm |

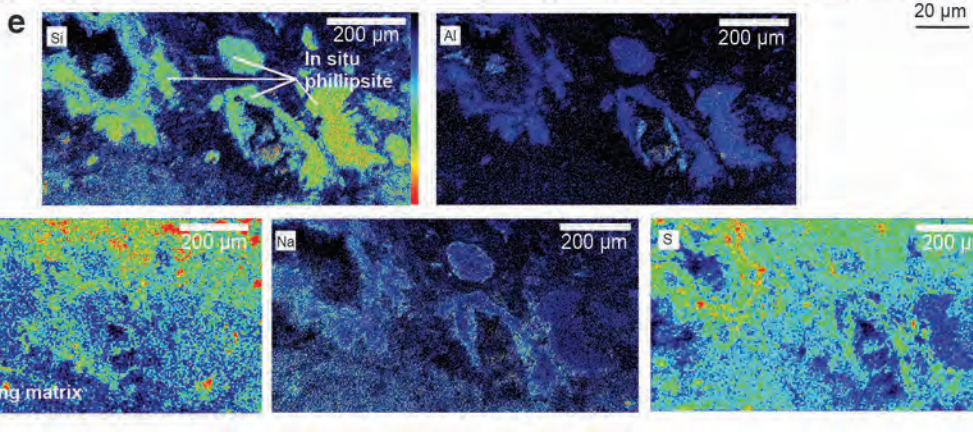

Figure 10

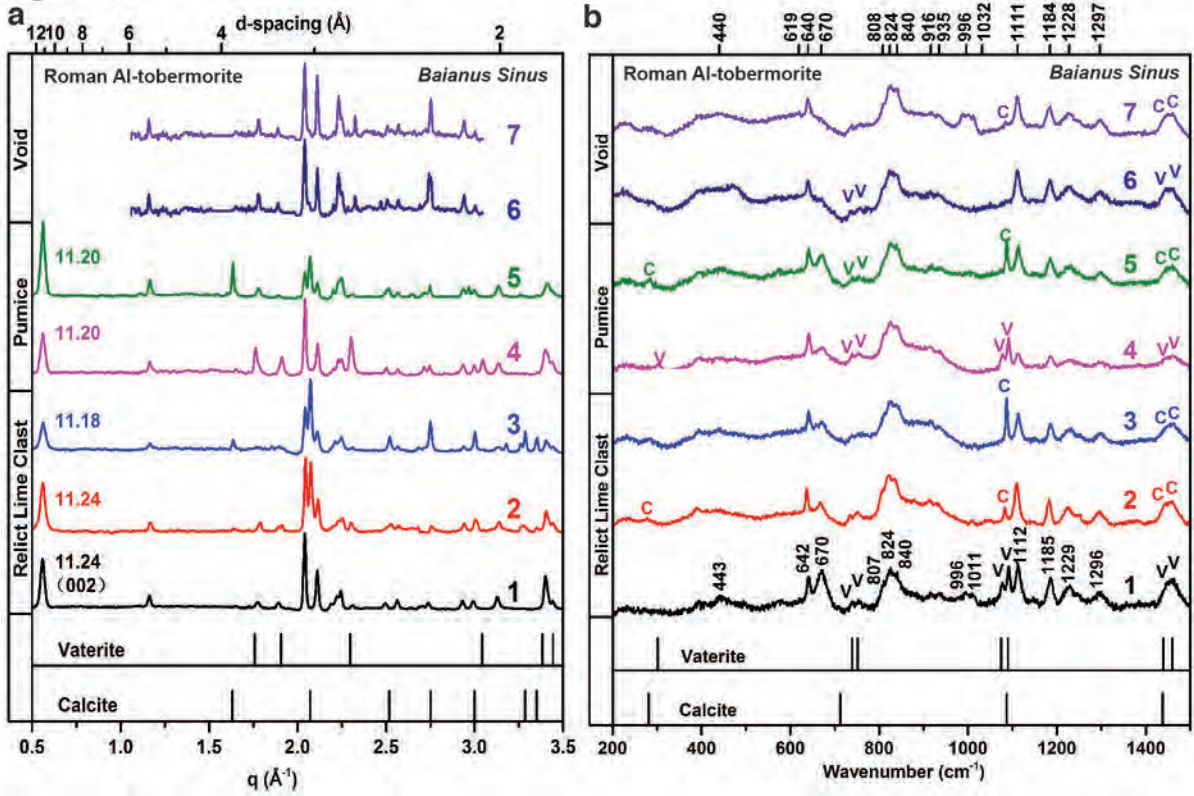
a
12
10
8
6
4
d-spacing (Å)
2
Roman Al-tobermorite
Baianus Sinus
Void
Pumice
Relict Lime Clast
7
6
11.20
5
11.20
4
11.18
3
11.24
2
11.24
(002)
1
Vaterite
Calcite
0.5
1.0
1.5
2.0
2.5
3.0
3.5
q (Å-1)
b
440
619
640
670
808
824
840
916
935
996
1032
1111
1184
1228
1297
Roman Al-tobermorite
Baianus Sinus
Void
Pumice
Relict Lime Clast
7
6
5
4
3
2
1
C
V
443
642
670
807
824
840
996
1011
1112
1185
1229
1296
Vaterite
Calcite
200
400
600
800
1000
1200
1400
Wavenumber (cm-1)

Figure 11

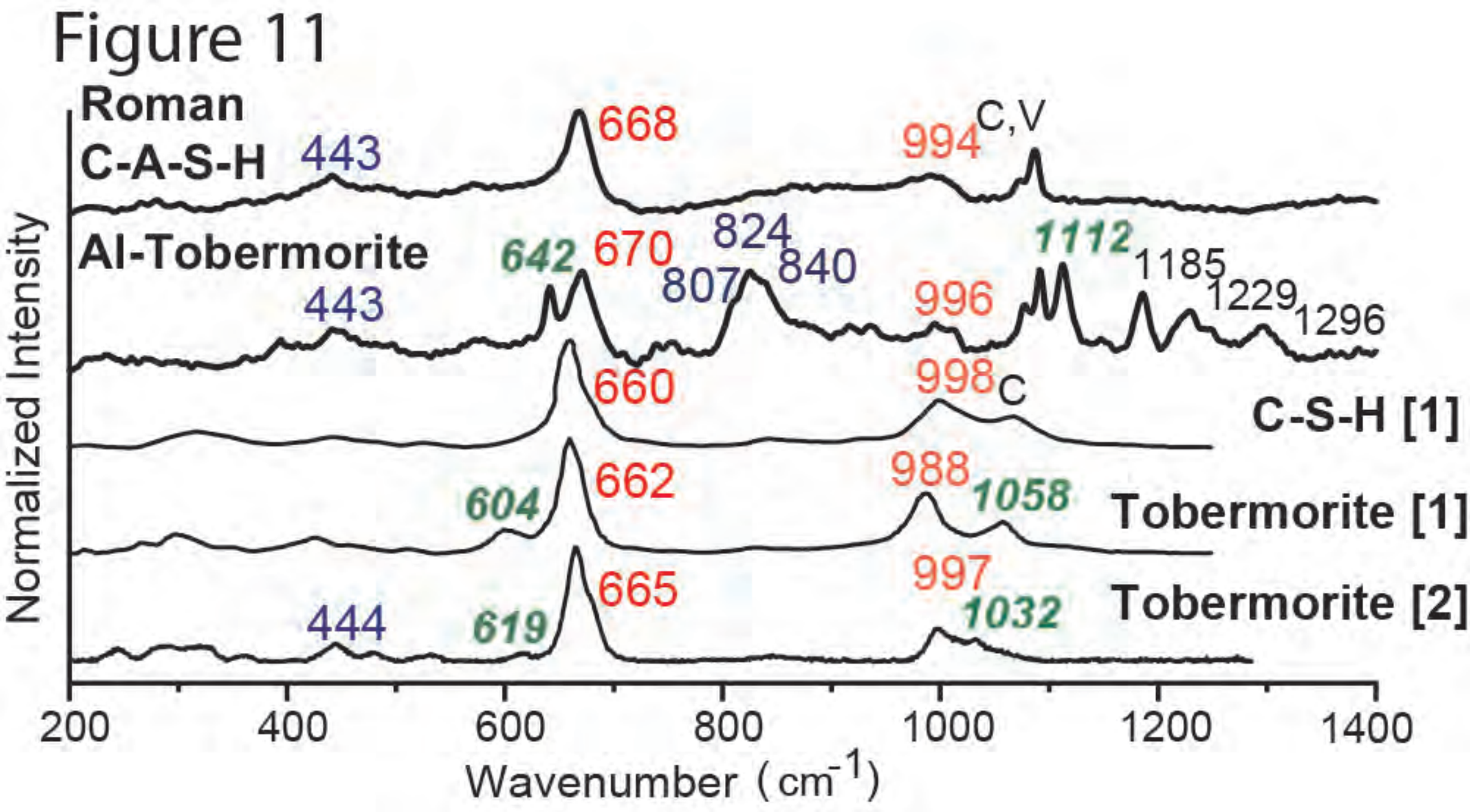
Roman
C-A-S-H
443
668
994
C,V
Al-Tobermorite
642
670
824
807
840
1112
1185
1229
1296
443
996
660
998
C
C-S-H [1]
604
662
988
1058
Tobermorite [1]
997
665
444
619
1032
Tobermorite [2]
Normalized Intensity
200
400
600
800
1000
1200
1400
Wavenumber (cm-1)

Figure 12

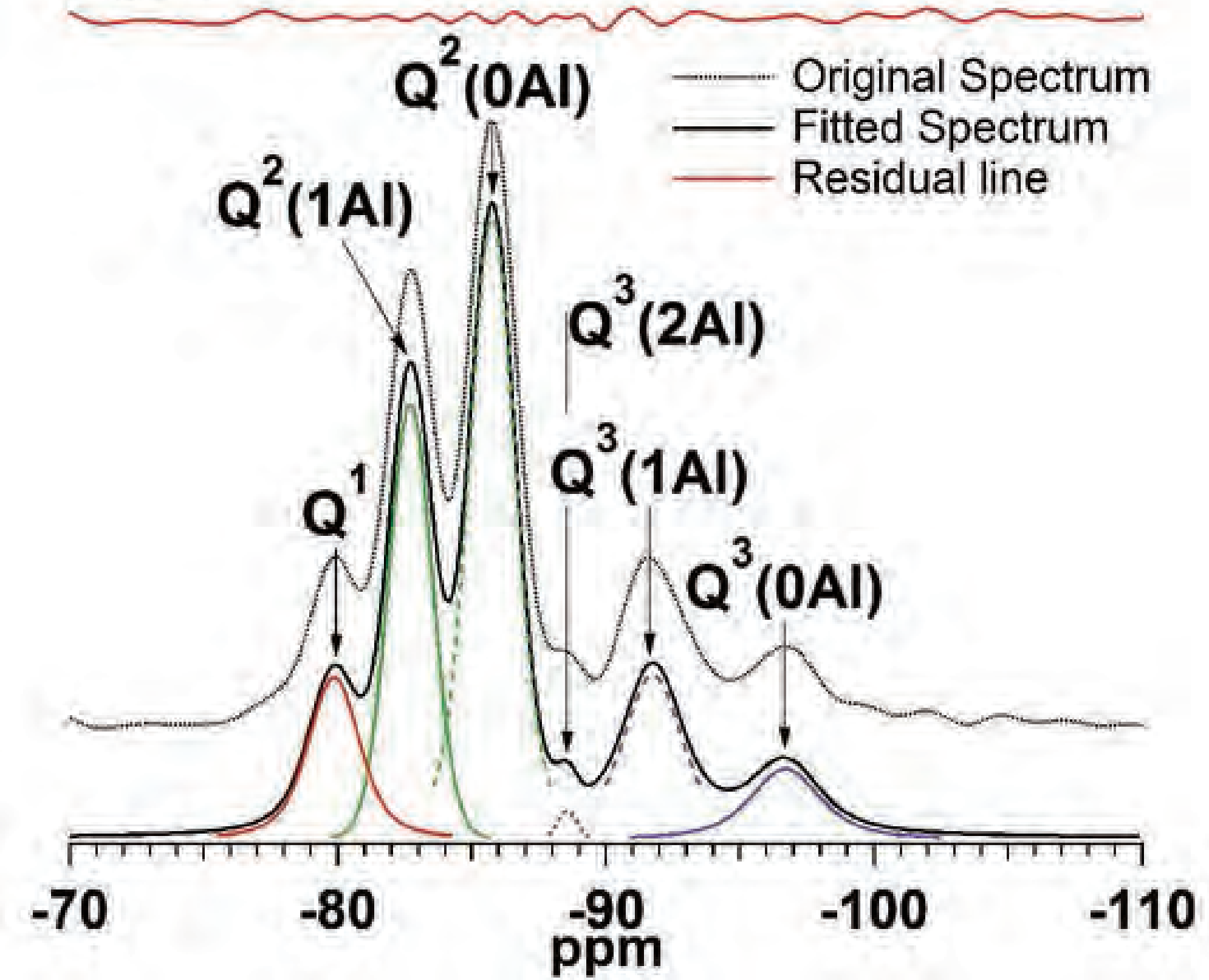
Q2(0Al)
Original Spectrum
Fitted Spectrum
Residual line
Q2(1Al)
Q3(2Al)
Q3(1Al)
Q1
Q3(0Al)
-70
-80
-90
-100
-110
ppm

**Table 1.** Phillipsite compositions measured by EPMA.

| | | | *Neapolitan Yellow Tuff* | | *Bacoli Tuff* (BRI.05.BT) | | *Baianus Sinus* (06-BAI-03) | | Portus Neronis (ANZ.02.01) | | | Portus Traianus (PTR.02.02) | | *Trajan* (GF |
|---|---|---|---|---|---|---|---|---|---|---|---|---|---|---|
| | | | | | Pumice | Void | Pumice | Void | Pumice | | | Void | | Tufo |
| | | | 1 | 3 | | | | | A | B | C | | | |
| **Weight% Oxide** | | | | | | | | | | | | | | |
| | LLD* | ±2σ‡ | | | | | | | | | | | | |
| $SiO_2$ | 0.04 | 0.45 | 53.1 | 52.0 | 58.6 | 58.8 | 46.7 | 39.5 | 57.3 | 56.1 | 60.2 | 46.0 | 50.1 | 49. |
| $TiO_2$ | 0.19 | 0.02 | 0.0 | 0.0 | 0.0 | 0.0 | 0.0 | 0.0 | 0.0 | 0.0 | 0.0 | 0.0 | 0.0 | 0. |
| $Al_2O_3$ | 0.04 | 0.24 | 22.3 | 23.7 | 20.2 | 19.3 | 22.8 | 27.6 | 20.9 | 18.6 | 20.2 | 21.4 | 23.4 | 20. |
| $Fe_2O_3$ | 0.14 | 0.08 | 0.2 | 0.0 | 0.0 | 0.2 | 0.3 | 0.0 | 0.3 | 0.3 | 0.0 | 0.2 | 0.0 | 0. |
| MnO | 0.13 | 0.01 | 0.0 | 0.0 | 0.0 | 0.0 | 0.0 | 0.0 | 0.0 | 0.0 | 0.0 | 0.0 | 0.2 | 0. |
| MgO | 0.02 | 0.01 | 0.0 | 0.0 | 0.0 | 0.0 | 0.0 | 0.0 | 0.2 | 0.0 | 0.0 | 0.1 | 0.0 | 0. |
| CaO | 0.03 | 0.16 | 7.6 | 8.2 | 1.1 | 0.4 | 2.0 | 10.7 | 1.3 | 0.9 | 1.0 | 4.8 | 4.1 | 4. |
| $Na_2O$ | 0.05 | 0.13 | 0.8 | 0.6 | 3.6 | 3.8 | 3.2 | 1.4 | 4.0 | 4.8 | 4.9 | 2.0 | 2.1 | 1. |
| $K_2O$ | 0.03 | 0.26 | 7.1 | 7.7 | 9.8 | 10.3 | 5.1 | 2.8 | 7.3 | 8.0 | 8.4 | 7.3 | 8.5 | 8. |
| Sum | | | 91.1 | 92.2 | 93.5 | 92.7 | 80.2 | 82.0 | 91.4 | 88.7 | 94.6 | 81.8 | 88.4 | 84. |
| $H_2O$† | | | 9.0 | 9.0 | 9.2 | 9.1 | 8.0 | 8.0 | 9.1 | 8.8 | 9.4 | 8.0 | 8.6 | 8. |
| **Number of atoms per formula unit based on 16O** | | | | | | | | | | | | | | |
| | | ±2σ‡ | | | | | | | | | | | | |
| Si | | 0.4 | 5.3 | 5.2 | 5.7 | 5.8 | 5.2 | 4.4 | 5.6 | 5.7 | 5.8 | 5.2 | 5.2 | 5. |
| Ti | | 0.0 | 0.0 | 0.0 | 0.0 | 0.0 | 0.0 | 0.0 | 0.0 | 0.0 | 0.0 | 0.0 | 0.0 | 0. |
| Al | | 0.2 | 2.6 | 2.8 | 2.3 | 2.2 | 3.0 | 3.7 | 2.4 | 2.2 | 2.3 | 2.8 | 2.9 | 2. |
| $Fe^{3+}$ | | 0.1 | 0.0 | 0.0 | 0.0 | 0.0 | 0.0 | 0.0 | 0.0 | 0.0 | 0.0 | 0.0 | 0.0 | 0. |
| Mn | | 0.0 | 0.0 | 0.0 | 0.0 | 0.0 | 0.0 | 0.0 | 0.0 | 0.0 | 0.0 | 0.0 | 0.0 | 0. |
| Mg | | 0.0 | 0.0 | 0.0 | 0.0 | 0.0 | 0.0 | 0.0 | 0.0 | 0.0 | 0.0 | 0.0 | 0.0 | 0. |
| Ca | | 0.2 | 0.8 | 0.9 | 0.1 | 0.0 | 0.2 | 1.3 | 0.1 | 0.1 | 0.1 | 0.6 | 0.5 | 0. |
| Na | | 0.1 | 0.2 | 0.1 | 0.7 | 0.7 | 0.7 | 0.3 | 0.8 | 0.9 | 0.9 | 0.4 | 0.4 | 0. |
| K | | 0.3 | 0.9 | 1.0 | 1.2 | 1.3 | 0.7 | 0.4 | 0.9 | 1.0 | 1.0 | 1.1 | 1.1 | 1. |
| Sum | | | 9.9 | 10.0 | 10.1 | 10.1 | 10.0 | 10.1 | 10.0 | 10.1 | 10.1 | 10.1 | 10.1 | 10. |

* 3σ lower limit of detection

** Calculated by stoichiometry

† Average absolute analytical uncertainty on the weight percent oxide

‡ Average absolute uncertainty on the number of atoms per formula unit, calculated following Giaramita and Day (1990).

**Table 2.** Al-tobermorite compositions from *Baianus Sinus* and *Portus Neronis* measured by EPMA.

| | | | *Baianus Sinus* (Bay of Pozzuoli, ROMACONS core BAI.06.03) | | | | | | | *Portus Neronis* (Anzio, ROMACONS core ANZ.02.01) | | | | | | |
|---|---|---|---|---|---|---|---|---|---|---|---|---|---|---|---|---|
| | | | Large Lime Clast | | Pumice Clast | | Lime Clast | | Void | Pumice Clast | | | | Pumice Clast | | |
| | | | LLP.1 | LLP.2 | PL.2 | PL.4 | PL.7 | PL.8 | Y.17S | A1 4 | | | | A1 6 | | |
| **Weight% Oxide** | | | | | | | | | | | | | | | | |
| | LLD* | ±2σ† | | | | | | | | | | | | | | |
| $SiO_2$ | 0.06 | 0.39 | 40.1 | 38.4 | 45.5 | 47.6 | 37.9 | 39.9 | 39.0 | 44.2 | 45.5 | 45.7 | 47.5 | 44.8 | 43.2 | 44.6 |
| $Al_2O_3$ | 0.03 | 0.15 | 6.7 | 6.2 | 6.8 | 6.1 | 6.7 | 5.6 | 5.5 | 6.9 | 7.1 | 7.3 | 7.4 | 4.3 | 4.3 | 4.4 |
| $Fe_2O_3$ | 0.19 | 0.07 | 0.0 | 0.0 | 0.0 | 0.0 | 0.2 | 0.0 | 0.0 | 0.0 | 0.3 | 0.3 | 0.3 | 0.0 | 0.0 | 0.0 |
| MgO | 0.02 | 0.04 | 0.1 | 0.2 | 0.0 | 0.0 | 0.3 | 0.3 | 0.0 | 0.1 | 0.2 | 0.1 | 0.2 | 0.0 | 0.0 | 0.0 |
| CaO | 0.05 | 0.49 | 34.5 | 32.7 | 34.1 | 34.5 | 32.5 | 33.4 | 32.1 | 29.0 | 25.8 | 24.2 | 23.5 | 30.2 | 31.2 | 31.7 |
| $Na_2O$ | 0.01 | 0.10 | 0.4 | 1.5 | 0.4 | 0.8 | 1.2 | 2.1 | 2.0 | 0.7 | 0.6 | 1.9 | 0.8 | 1.4 | 2.3 | 1.5 |
| $K_2O$ | 0.03 | 0.09 | 0.6 | 1.0 | 0.8 | 1.0 | 0.7 | 0.6 | 0.9 | 1.1 | 0.9 | 1.6 | 1.4 | 0.4 | 0.7 | 0.5 |
| Sum | | 0.68 | 82.4 | 79.9 | 87.6 | 89.9 | 79.5 | 81.8 | 79.5 | 81.9 | 80.4 | 81.0 | 81.2 | 81.0 | 81.7 | 82.7 |
| $H_2O$** | | | 12.2 | 11.7 | 13.2 | 13.5 | 11.7 | 12.0 | 11.7 | 11.8 | 11.8 | 11.9 | 12.1 | 11.7 | 11.6 | 11.8 |
| **Number of atoms per formula unit based on 18[O, (OH)]** | | | | | | | | | | | | | | | | |
| | | ±2σ‡ | | | | | | | | | | | | | | |
| Si | | 0.03 | 4.9 | 4.9 | 5.2 | 5.3 | 4.9 | 5.0 | 5.0 | 5.3 | 5.5 | 5.5 | 5.6 | 5.5 | 5.3 | 5.4 |
| Al | | 0.02 | 1.0 | 0.9 | 0.9 | 0.8 | 1.0 | 0.8 | 0.8 | 1.0 | 1.0 | 1.0 | 1.0 | 0.6 | 0.6 | 0.6 |
| $Fe^{3+}$ | | 0.01 | 0.0 | 0.0 | 0.0 | 0.0 | 0.0 | 0.0 | 0.0 | 0.0 | 0.0 | 0.0 | 0.0 | 0.0 | 0.0 | 0.0 |
| Mg | | 0.01 | 0.0 | 0.0 | 0.0 | 0.0 | 0.0 | 0.1 | 0.0 | 0.0 | 0.0 | 0.0 | 0.0 | 0.0 | 0.0 | 0.0 |
| Ca | | 0.05 | 4.6 | 4.5 | 4.2 | 4.1 | 4.5 | 4.5 | 4.4 | 3.7 | 3.3 | 3.1 | 3.0 | 3.9 | 4.1 | 4.1 |
| Na | | 0.02 | 0.1 | 0.4 | 0.1 | 0.2 | 0.3 | 0.5 | 0.5 | 0.2 | 0.1 | 0.4 | 0.2 | 0.3 | 0.5 | 0.4 |
| K | | 0.01 | 0.1 | 0.2 | 0.1 | 0.1 | 0.1 | 0.1 | 0.1 | 0.2 | 0.1 | 0.2 | 0.2 | 0.1 | 0.1 | 0.1 |
| Sum | | 0.03 | 10.7 | 10.9 | 10.5 | 10.5 | 10.8 | 10.9 | 10.9 | 10.4 | 10.1 | 10.3 | 10.1 | 10.4 | 10.7 | 10.5 |
| **Cation ratios** | | | | | | | | | | | | | | | | |
| Ca/(Al+Si) | | | 0.77 | 0.77 | 0.68 | 0.67 | 0.76 | 0.77 | 0.76 | 0.59 | 0.51 | 0.48 | 0.45 | 0.65 | 0.69 | 0.68 |
| Al/(Al+Si) | | | 0.16 | 0.16 | 0.15 | 0.13 | 0.17 | 0.14 | 0.14 | 0.15 | 0.16 | 0.16 | 0.15 | 0.10 | 0.10 | 0.11 |

* 3σ lower limit of detection

** Calculated by stoichiometry

† Average absolute analytical uncertainty on the weight percent oxide

‡ Average absolute uncertainty on the number of atoms per formula unit, calculated following Giaramita and Day (1990)

**Table 3.** Assignments of Raman frequency shifts to silicate and aluminate linkages in *Baianus Sinus* C-A-S-H and Al-tobermorite compared with previous studies of C-S-H and tobermorite.

| Previous Studies | | | | *Baianus Sinus* mortar | | Inferred Linkage [*,†,**] |
|---|---|---|---|---|---|---|
| Frequency ($cm^{-1}$) | | | Assignment | Frequency ($cm^{-1}$) | | |
| C-S-H[*,†] Ca/Si=0.83 | 11Å Tobermorite | | | C-A-S-H Ca/(Si+Al)≈0.8[¶] | 11Å Al-Tobermorite | |
| | * | † | | | | |
| 441–540 | 421 | 444 | $\nu_2(SiO_4)$ Internal Deformations | 442–451 | 428–443 | — |
| 600–630 | 604 | 619 | $\nu_4(SiO_4)$ Symmetric Bending | — | 638–642[7] | SB $Q^3$ (0Al)<br>SB $Q^3$ (1Al) |
| 660–680[*,†,‡,§] | 662 | 665 | 600–700 | 668–671 | 670–671 | SB $Q^2$ (0Al)<br>SB $Q^2$ (1Al) |
| 850 | — | — | $\nu_1(SiO_4)$ Symmetric Stretching 800–1200 | — | 806–809<br>821–826<br>837–842<br>(840–900) | SS $Q^1$ (0Al)<br>SS $Q^1$(1Al)<br>SS Al–O[**,††] |
| 998–1010[‖] | 988 | 997 | | 996 | (913-1012)[‖] | SS $Q^2$ (0Al)<br>SS $Q^2$ (1Al) |
| 1040–1114 | 1058 | 1032 | | (1068 vaterite) | 1110–1113 | SS $Q^3$ (0Al)[‡‡]<br>SS $Q^3$ (1Al) |
| | | | to be determined | | 1228<br>1250<br>1297 | |

* Kirkpatrick et al. 1997

† Richardson et al. 2010

‡ http://rruff.info/Tobermorite R060147, Crestmore Quarries, Riverside, CA

§ Black et al. 2007

|| Black 2009, 950-1000 $cm^{-1}$ band is also attributed to anti-symmetric stretching of $Q^2$ silicate linkages.

¶ Jackson et al. 2013

# Frost et al. 1998, FT-Raman analysis of kaolinite, 645 band records SS of ($SiO_4$) tetrahedral units when the incident laser beam is directed parallel to the c-axis of layered crystals.

l Weak bands at 913-918, 934-93, 990-1000, 1000-1012.

†† McMillan and Piriou, 1982

‡‡ Sharma et al. 1982, 655 band in gehlenite reflects vibrational modes of $AlO_4$ tetrahedra.

§§ Wehrmeister et al. 2010, vaterite and calcite bands obscure silicate stretching